Journal of Alloys and Compounds 913 (2022) 165145

Contents lists available at ScienceDirect

Journal of Alloys and Compounds

journal homepage: www.elsevier.com/locate/jalcom

Effects of different zinc oxide morphologies on photocatalytic desulfurization of thiophene

Ummi Kalsum Hasanah Mohd Nadzim[a], Nur Hanis Hayati Hairom[a,b,*], Mohamad Alif Hakimi Hamdan[a], Mohd Khairul Ahmad[b], Aishah Abdul Jalil[c,d], Nurfatehah Wahyuny Che Jusoh[e], Sofiah Hamzah[f]

[a] Faculty of Engineering Technology, Universiti Tun Hussein Onn Malaysia, Hab Pendidikan Tinggi Pagoh, Km 1, Jalan Panchor, 84600 Muar, Johor, Malaysia
[b] Microelectronics and Nanotechnology-Shamsuddin Research Center, Institute for Integrated Engineering, Universiti Tun Hussein Onn Malaysia, Parit Raja, 86400 Batu Pahat, Johor, Malaysia
[c] School of Chemical and Energy Engineering, Faculty of Engineering, Universiti Teknologi Malaysia, 81310 UTM Johor Bahru, Johor, Malaysia
[d] Centre of Hydrogen Energy, Institute of Future Energy, 81310 UTM Johor Bahru, Johor, Malaysia
[e] Department of Chemical Process Engineering, Malaysia-Japan International Institute of Technology (MJIIT), Universiti Teknologi Malaysia Kuala Lumpur, Jalan Sultan Yahya Petra, 54100 Kuala Lumpur, Malaysia,
[f] Environmental Sustainable Material Research Interest Group, Faculty of Ocean Engineering Technology & Informatics, Universiti Malaysia Terengganu, 21030 Kuala Nerus, Terengganu, Malaysia

ARTICLE INFO

Article history:
Received 6 February 2022
Received in revised form 13 April 2022
Accepted 21 April 2022
Available online 26 April 2022

Keywords:
Desulfurization
Photocatalyst
Thiophene
Zinc oxide

ABSTRACT

Zinc oxide (ZnO) nanoparticles are superior photocatalysts for pollutant degradation due to their stability, low hazard, and high photosensitivity. The morphology of this material is one of the key factors influencing the performance of pollutant degradation. In fact, studies on the effects of different ZnO morphologies on thiophene desulfurization via photocatalysis process are limited. Thus, this study focuses on the performance of different ZnO morphologies for thiophene desulfurization. Nine ZnO nanoparticles were synthesized and categorized into two groups, namely flower-like and non-flower-like ZnO. Flower-like ZnO included flakes, clusters, rods, and needles, while the non-flower-like ZnO comprised nanoballs, short-nanorods, nanocubes, and nanoporous. The physical properties of all ZnO morphologies were characterized using X-ray diffraction (XRD), field emission scanning electron microscopy (FESEM), and Fourier-transform infrared (FTIR), and compared with commercial ZnO. From the findings, flower-like ZnO flakes showed the highest performance in thiophene desulfurization (30%). High pH and turbidity reduction in the permeate confirmed that the thiophene compound in the solution was highly degraded after treatment. Moreover, all ZnO morphologies applied to pseudo-second-order models due to higher linear regression (R^2) values. Greater thiophene desulfurization was indicated by the highest Ce value of ZnO flakes (909.09 mg/g). The optimum conditions for thiophene desulfurization were at pH 7 and 0.05 g/L ZnO flakes loading for 90 min contact time.

1. Introduction

The petroleum industry is one of the largest industries in Malaysia and is a vital part of the national economy. Despite its high revenue to the country, this industry is vulnerable as it contributes to substantial environmental pollution. In petroleum, sulfur is the third most abundant element after carbon and hydrogen that contributes to air pollution stemming from the production of SO_2 species known as toxic gas during combustion [1]. In addition, thiophene is one of the sulfur-containing compounds (SCCs) in petroleum with a simple aromatic compound containing sulfur atom (C_4H_4S). It belongs to heterocyclic compounds as it is structured as five-member rings consisting of one heteroatom, namely sulfur [2]. Moreover, thiophene is a toxic and flammable aromatic compound where the production of toxic oxides during combustion can lead to adverse impacts on the environment [3]. This compound can also cause severe reactor and equipment corrosion during oil processing. In conventional technology, hydrodesulfurization (HDS) is employed but is still ineffective for removing thiophene due to its stable

* Corresponding author at: Faculty of Engineering Technology, Universiti Tun Hussein Onn Malaysia, Hab Pendidikan Tinggi Pagoh, Km 1, Jalan Panchor, 84600 Muar, Johor, Malaysia.
E-mail address: nhanis@uthm.edu.my (N.H.H. Hairom).

https://doi.org/10.1016/j.jallcom.2022.165145
0925-8388/

aromatic compound. This technology is also expensive as it entails high hydrogen consumption, high temperature (~450 °C), high hydrogen pressure (~200 bar) [4], and more active catalysts to achieve deep desulfurization. Therefore, advanced desulfurization such as photocatalysis technology is required to address the above-mentioned issues.

In recent years, the photocatalysis process has attracted vast attention for environmental purification and treatment including thiophene desulfurization as it is more environmentally friendly. Photocatalysis is favorable for organic degradation in an aqueous system as a low-cost and non-toxic method [5,6]. Metal oxides are the best photocatalysts commonly used for photocatalysis process due to their ability to absorb light and oxidize organic pollutants [7]. Zinc oxide (ZnO) nanoparticles are one of the most commonly used semiconductor metal oxides in photocatalysis as they are more stable, photosensitive economically, and have higher H_2O_2 generation compared to others [8]. It has a direct wide bandgap of 3.37 eV and a large excitation binding energy of 60 meV [9], which is widely applied in piezoelectric nanogenerators, dye-sensitized solar cells, biodevices, optoelectronic nanodevices, and photocatalyst for degradation and removal of environmental pollutants. The wurtzite structure of ZnO allows a large exciton binding energy to generate ultraviolet (UV) light efficiency at standard temperatures.

In terms of application, ZnO has exhibited immense potential in photoelectrical devices as reported by several researchers. For instance, Zang [10] demonstrated an increase in power conversion efficiency up to 60.6% for ZnO/Cu_2O solar cells with well-oriented micrometer grain-sized Cu_2O films. Wang et al. [11] employed NH_4Cl-modified ZnO to enhance the performance of CsPbIBr2 perovskite solar cells for electron transport layer (ETL) via low temperature process. By tuning the surface morphology of the perovskite film, the open-circuit voltage (V_{OC}) was increased, severe hysteresis was reduced and the device stability was improved. On another note, Wang et al. [12] reported that the use of ZnO nanorods arrays as an ETL enhanced the performance of CsPbBr3 quantum dots photodetectors in terms of on/off ratio, fast response time and low responsivity. The application of ZnO as photocatalyst in the degradation of pollutant is also outstanding. In a study conducted by Meshram et al. [13], ZnO-bentonite composite was employed to remove phenol from simulated effluent. Using a continuous stirred tank reactor (CSTR), the removal of phenol achieved ~70% at a lower flow rate of 10 mL min^{-1} and higher pH (12) at fixed nanocomposite loading. In addition, ZnO has been applied in treating industrial dye wastewater via membrane photocatalytic reactor (MPR) [14]. The treatment performance was found to be better when incorporated with ZnO and assisted by nanofiltration membrane, where the color removal of the dye was 100%. In another study, the performance of MPR was enhanced in treating palm oil mill secondary effluent (POMSE) with the use of ZnO-*Cymbopogon citratus* (ZnO-CC) [15]. Chemical oxygen demand, biochemical oxygen demand and turbidity of POMSE was removed efficiently by 98–99%.

Furthermore, several previous studies have reported that thiophene has been successfully desulfurized via photocatalysis process using Ag-$BiVO_4$ [16], cube-like Cu/Cu_2O/$BiVO_4$/Bi_7VO_{13} [1], TiO_2 [17], and p-BiOI/n-BiPO4 [18] as photocatalysts. However, the method of preparation of photocatalysts is strenuous, consumes high heavy metal levels and the chemical reagent costs is high when utilized on an industrial scale. Moreover, the air/oxygen supply to the system over a longer period can affect capital costs for industrial scale [3]. In addition, the morphology of ZnO is crucial to examine to solve agglomeration and aggregation problems as well as to improve surface active sites and light absorption. By improving the morphology and surface area, the efficiency of photocatalytic activities can be enhanced [19]. According to Karthikeyan et al. [20], the key factors influencing the photocatalytic properties are the specific surface area, bandgap energy, and morphology of the materials.

Therefore, controlling the size and shape of these nanostructures during synthesis is the main focus of this study. Preparation of ZnO with different morphologies (flower-like and non-flower-like) at different conditions via simple and less hazardous routes, i.e., hydrothermal and chemical bath deposition methods, was performed in this study for photo-desulfurization of thiophene. The physicochemical properties of these ZnO morphologies were also characterized for a comprehensive understanding. This study also investigated the best-performing ZnO morphology for thiophene desulfurization via a photocatalytic reactor rig. The outcome of this study provides an elucidation of the performance of different ZnO morphologies for desulfurization of thiophene to develop advanced sulfur treatment systems that have the potential to comply with the permissible limit of sulfur-containing compounds worldwide.

2. Material and method

2.1. Synthetic sulfur pollutants

Experimental work was initiated by preparing synthetic sulfur pollutant. To prepare 300 ppm of sulfur pollutant content, 0.1429 mL of synthetic thiophene was dissolved in 500 mL of acetonitrile solution. Both chemicals were purchased from Sigma-Aldrich, Merk KGaA, Germany, and used without further purification.

2.2. Synthesis of ZnO photocatalysts under different conditions

The chemicals used were 0.5 M and 1 M of sodium hydroxide (NaOH), 0.5 M of zinc acetate dihydrate ($Zn(C_2H_3O_2)_2$•$2H_2O$), 0.5 M of zinc nitrate hexahydrate ($Zn(NO_3)_2$•$6H_2O$), 0.5 M and 1 M of hexamethylenetetramine (HMTA) (CH_2)$6N_4$, and ethanol. All chemicals were purchased from R&M Marketing, Essex, UK, and used without further purification.

2.2.1. Synthesis via hydrothermal method

Flower-like ZnO flakes, and clusters, as well as non-flower-like ZnO nanoballs, short-nanorods, nanocubes, and nanoporous were synthesized via hydrothermal method. To synthesize flower-like ZnO flakes, about 0.5 M of $Zn(C_2H_3O_2)_2$•$2H_2O$ and 0.5 M of HMTA (CH_2)$6N_4$ were prepared using deionized water as a solvent, separately. After that, 0.5 M of HMTA solution was gradually added into 0.5 M of $Zn(C_2H_3O_2)_2$•$2H_2O$ solution. The mixed solution was stirred at room temperature for several minutes until it achieved homogeneity. Under continuous stirring, the pH of the mixed solution was adjusted to 12 and continued stirring for 20 min. The pH of the solution was adjusted using 0.5 M NaOH. Next, the mixture was transferred into 300 mL of Teflon lined stainless steel autoclave and heated in an oven at 150 °C for 3 h.

After 3 h, the autoclave was allowed to cool to room temperature. The white precipitate formed was filtered and washed several times with deionized water, followed by rinsing with ethanol. Then, the filtered product was dried at 90 °C for 1 h in the oven to remove moisture. The obtained samples were calcined in the furnace at 550 °C for 2 h to remove any impurities in the samples. Flower-like ZnO flakes were produced in the form of white powder and collected for further analysis. Similar procedures were employed for the synthesis of other ZnO morphologies. However, the chemical precursor, pH, temperature, and autoclave time were varied accordingly as summarized in Table 1.

2.2.2. Synthesis via chemical bath deposition method

Moreover, chemical bath deposition (CBD) method was employed for the synthesis of flower-like ZnO rods and needles. For rod morphology, about 0.02 M of ($Zn(C_2H_3O_2)_2$•$2H_2O$) and 0.04 M of HMTA (CH_2)$6N_4$ were prepared using deionized water as a solvent, separately. After that, 0.04 M of HMTA solution was gradually added

Table 1
Summary of ZnO photocatalyst preparation methods.

Morphology	Type	Method	Condition			
			Chemical precursor	pH	Temp. (°C)	Time (h)	Furnace
Flower-like ZnO	Flakes	Hydrothermal	0.5 M ZnAc + 0.5 M HMTA	12	150	3	Yes
	Cluster	Hydrothermal	0.5 M ZnNit + 1 M HMTA	6	100	5	Yes
	Rods	Chemical bath deposition	0.02 M ZnAc + 0.04 M HMTA	7	90	1	Yes
	Needles	Chemical bath deposition	0.02 M ZnNit + 0.04 M HMTA	6	90	1	Yes
Non-flower-like ZnO	Nanoball	Hydrothermal	0.5 M ZnAc + 1 M NaOH	11	100	3	Yes
	Short-nanorods	Hydrothermal	0.5 M ZnAc + 0.5 M HMTA	11	100	3	Yes
	Nano-cubes	Hydrothermal	0.5 M ZnAc + 0.5 M HMTA	11	100	10	Yes
	Nano-porous	Hydrothermal	0.5 M ZnAc + 1 M HMTA	7	100	5	Yes

Notes: ZnAc – zinc acetate dihydrate; ZnNit – zinc nitrate hexahydrate; HMTA – hexamethylenetetramine; NaOH – sodium oxide.

into 0.02 M of $Zn(C_2H_3O_2)_2$•$2H_2O$ solution. At room temperature, the mixed solution was stirred continuously for several minutes until homogeneous. The temperature of the mixed solution increased gradually to 90–95 °C and maintained for 1 h. After the reaction was completed, the mixed solution was allowed to cool to room temperature. Then, the white precipitate formed was filtered using filter paper and collected. The precipitate was washed with deionized water and ethanol several times. Finally, the product was oven-dried below 90 °C for 1 h to form a powder. The obtained samples were calcined in the furnace below 550 °C for 2 h to remove any impurities in the samples. Flower-like ZnO rods were produced in the form of white powder and collected for further analysis. Using the same method, synthesis of needle morphology was performed. However, the chemical precursor was converted to $Zn(NO_3)_2$•$6H_2O$ and the pH of the solution was also adjusted as summarized in Table 1.

2.3. Characterization of ZnO photocatalysts

2.3.1. X-ray diffractometer (XRD)

Prior to characterization, flower-like ZnO samples were ground using a mortar to obtain a fine surface and size. Then, a zero-diffraction plate was cleaned, dried, and sterilized using ethanol. The ground samples were filled in clean zero diffraction plate. After that, the plate filled with samples was placed in XRD (Bruker AXSGmbH model) to investigate the sample crystallinity with Cu-Kα radiation of 1.54 Å, within 2θ angle ranging from 25 to 70. The results obtained were analyzed and represented in XRD pattern form. Moreover, the crystallite size of the ZnO samples was calculated according to Scherrer's formula [21].

$$\text{Crystallite size} = 0.94\lambda / \beta\cos\theta \quad (1)$$

where, λ = 1.54056 Å, β is full width at half maximum (FWHM) of an hkl peak at θ value.

2.3.2. Field emission scanning electron microscope (FESEM)

The surface morphology of various flower-like ZnO types was investigated using JEOL JSM-7600F FESEM with 300x – 50,000x magnification. For the preparation procedure, the sample stubs were cleaned and sterilized with ethanol. The conductive double-coated carbon tapes were pasted on the stubs. Then, flower-like ZnO samples were dispersed on the tapes carefully, gently, and in small amounts. Then, the stubs containing the samples were coated with a thin layer of copper using a coating machine for 20 min and then analyzed.

2.3.3. Fourier transform infrared (FTIR)

The composition and quality of the synthesized flower-like ZnO were characterized by Cary 600 series FTIR spectrometer at room temperature with a spectral resolution of 8 cm^{-1} and 16 scans in open beam air background in the mid-IR region (500–4000 cm^{-1}). For sample preparation, tapered shoes were fitted into the pressure knob and the powder was placed on the mounting plate properly. The plate was filled with 2–3 scoops of flower-like ZnO samples. Then, the lever was pulled gently. The sample was compacted by the force applied by turning the knob. The scan button was clicked and the sample was scanned by the software. The monitor displayed information based on selected peaks in the form of a graph. Finally, the sample was removed and the powder plate was cleaned using tissue and sterilized with ethanol. Characterization steps were repeated for other ZnO powders.

2.4. Photo-desulfurization of thiophene in the presence of different types of flower-like ZnO

Desulfurization of thiophene was conducted in a photocatalytic reactor rig as illustrated in Fig. 1. The reactor capacity was 2 L and equipped with quartz glass to hold an ultraviolet (UV) lamp (253.7 nm, 83 W, Daihan Scientific, Korea). To begin with, the initial pH of the prepared synthetic sulfur pollutant solution was measured and adjusted to pH 6. After that, 500 mL of the modified synthetic sulfur pollutant solution was transferred into the reactor. Then, 0.05 g/L of flower-like ZnO powder was added. The impeller equipped with an overhead stirrer (WiseStir HS-30D) was agitated at 250 rpm and constant temperature (25 °C) for 30 min to allow the adsorption and desorption processes to occur. Then, the UV lamp was turned on to induce the photocatalytic degradation process.

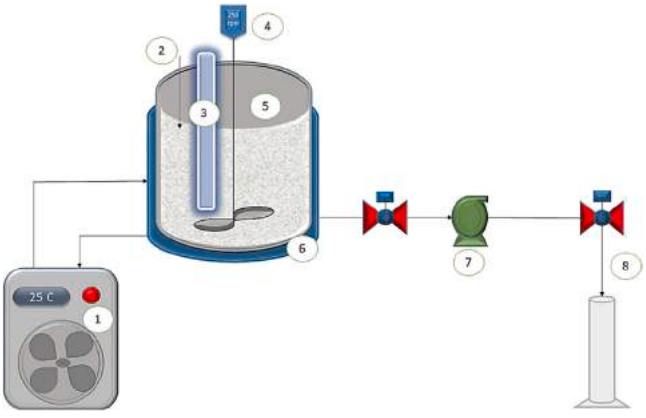

1	Chiller	2	Feed
3	UV lamp	4	Agitator motor
5	Reactor tank	6	Cooling jacket
7	Pump	8	Drain flow

Fig. 1. Schematic diagram of photocatalytic reactor rig.

After 5 min, the photocatalytic reactor valve was opened to drain out 10 mL of sample for UV–Vis analysis. Permeate samples were collected every 5 min for 90 min. Next, the permeate samples were centrifuged (Eppendorf, 5804 model) in 20 min to separate the photocatalyst from the permeate and used for further analysis [8,15,16]. The treatment procedure was repeated several times to determine the optimum conditions and to study the performance of various types of flower-like ZnO photocatalysts at various loadings (0.04, 0.05, 0.06 g/L), initial pH (6, 7, 8), and treatment period (5 h) [8,17].

2.5. Analysis of permeate

2.5.1. Desulfurization efficiency

Concentrations of sulfur pollutant solutions before and after treatment were measured and analyzed using UV–Vis spectrophotometer (LABOMED, INC, Spectro UV-2650). The UV absorption spectrum of thiophene are between 225 and 246 nm. According to Bucci et al. [22], the absorbance of 233 nm is the suitable wavelength for determining and measuring thiophene via UV–Vis spectrophotometer. The efficiency of desulfurization was calculated based on the following equation [23]:

$$\text{Desulfurization (\%), n} = (1 - C/Co) \times 100\% \quad (2)$$

where, C is the concentration of sulfur pollutant solution after treatment, and Co is the initial concentration of sulfur pollutant solution (before treatment). A comparison on permeate quality was made by plotting the percentage of desulfurization efficiency against operating time. Therefore, optimum conditions were obtained.

2.5.2. pH

The pH of permeate was measured using Merck pH indicator paper purchased from Merck, Germany. The pH paper was dipped into the permeate and matched to a scale provided to measure the pH value.

2.5.3. Turbidity

The turbidity of permeates was measured using HACH turbidimeter according to the standard procedure of HACH. To begin with, the operating range on the “AUTO” mode on the turbidimeter was selected. A clean sample cell was filled with test samples and placed in the cell holder. The outer part of the cell was wiped with lens tissue and the dot was aligned on the sample cell with an embossed mark on the spill ring around the opening of the cell holder. The cell was ensured to be kept underneath completely and held in place with a spring clip. The sample was covered with a light shield. Digital reading of values in Nephelometric Turbidity Unit (NTU).

2.6. Kinetic study of photo-desulfurization

The kinetic study of photocatalytic desulfurization investigated the reaction rate and performance of synthesized ZnO as photocatalyst for desulfurization of thiophene. Pseudo-first-order and second-order kinetic reactions were selected to calculate and identify the rate constants, k, as well as to evaluate the rate of reaction [24].

1) Pseudo-first-order model:

$$\ln(C_e - C_t) = \ln C_e - Kt \quad (3)$$

A graph of $\ln(C_e\text{-}C_t)$ against t was plotted. From the slope, the rate constant, k, was determined. Then, the reaction rate of thiophene desulfurization was calculated and the performance of the synthesized ZnO photocatalyst was evaluated.

2) Pseudo-second-order model:

$$\frac{t}{C_t} = \frac{1}{KC_e^2} + \frac{t}{C_e} \quad (4)$$

A graph of t/C_t against t was plotted. From the slope, the rate constant, k, was successfully determined. The reaction rate of thiophene desulfurization was calculated and the performance of the synthesized ZnO photocatalyst was evaluated.

3. Results and discussion

3.1. Characterization of ZnO with different morphologies

From the experiments, it was found that the morphology of ZnO could be categorized into flower-like and non-flower-like. The flower-like shape indicated that the morphology of ZnO was in the structure of the flower, i.e., flakes, clusters, rods, and needles. Meanwhile, the non-flower-like shape depicted the morphology of ZnO in other structures such as short-nanorods, nanocubes, nanoporous, and nanoballs, as opposed to flower-like structure. For in-depth study, the physicochemical properties of the synthesized ZnO were characterized using XRD, FESEM, and FTIR. The data obtained are further analyzed and discussed.

The use of hydrothermal and chemical bath deposition method was found to be suitable to control the morphological variation of ZnO. According to Udom [25], the hydrothermal method is extensively used as it is considered simple, scalable and efficient as well as facilitates the production of quality nanoscale crystalline for ZnO as a photocatalyst. This method has gained great popularity due to its tolerable growth conditions of ZnO nanostructures [26]. On the other hand, the chemical bath deposition method is advantageous it can produce good precipitate on a suitable substrate with controlled compound precipitation from the solution [27]. It can also control growth factors easily such as deposition rate, film thickness, and crystallites quality by changing the pH, temperature and bath concentration of the solution [28].

3.1.1. XRD analysis of synthesized ZnO

Fig. 2 depicts the XRD patterns for synthesized ZnO. The diffractograms for all samples were similar to those of commercial ZnO (Fig. 2(i)) and standard ZnO (Fig. 2(j)) peaks, which corresponded well to typical single-crystalline wurtzite hexagonal phase bulk of ZnO. The crystalline regions of all samples were observed to be in the range of 30° to 40° (2θ values). In addition, the XRD patterns corresponded well to the standard wurtzite structure on (1 0 0), (0 0 2), and (1 0 1) planes. The strong and sharp peaks exhibited good crystallinity of the synthesized materials. It also revealed that the flower-like ZnO rods had a higher and narrower shape from 30° to 40° compared to the others, indicating that the formers had higher crystallinity and lower surface defects. Moreover, less intense peaks were observed in the range of 45° to 70° for all samples, indicating high crystallinity in different forms [29]. Furthermore, no characteristic peaks of other impurities were detected in the pattern, signifying that all samples were successfully synthesized with high purity despite different preparation methods.

According to Table 2, the ascending order of crystallite size is as follows: ZnO nanoballs < nanocubes < nanoporous < flower-like flakes < short-nanorods < flower-like needles < flower-like clusters < flower-like rods < commercial ZnO. Particles were formed due to the combination of several grains and these grains were formed from the combination of several crystallites. For example, crystallite size ≤ grain size ≤ particle sizes [30]. Based on the results, the flower-like rods have a higher crystallite size than other synthesized ZnOs, indicating that the rods have higher grain size leading to larger particle size. This was supported by the XRD patterns, where the flower-like rods exhibited higher and narrower shapes in the range of 30° to 40° compared to others. For nanoballs, it has the smallest

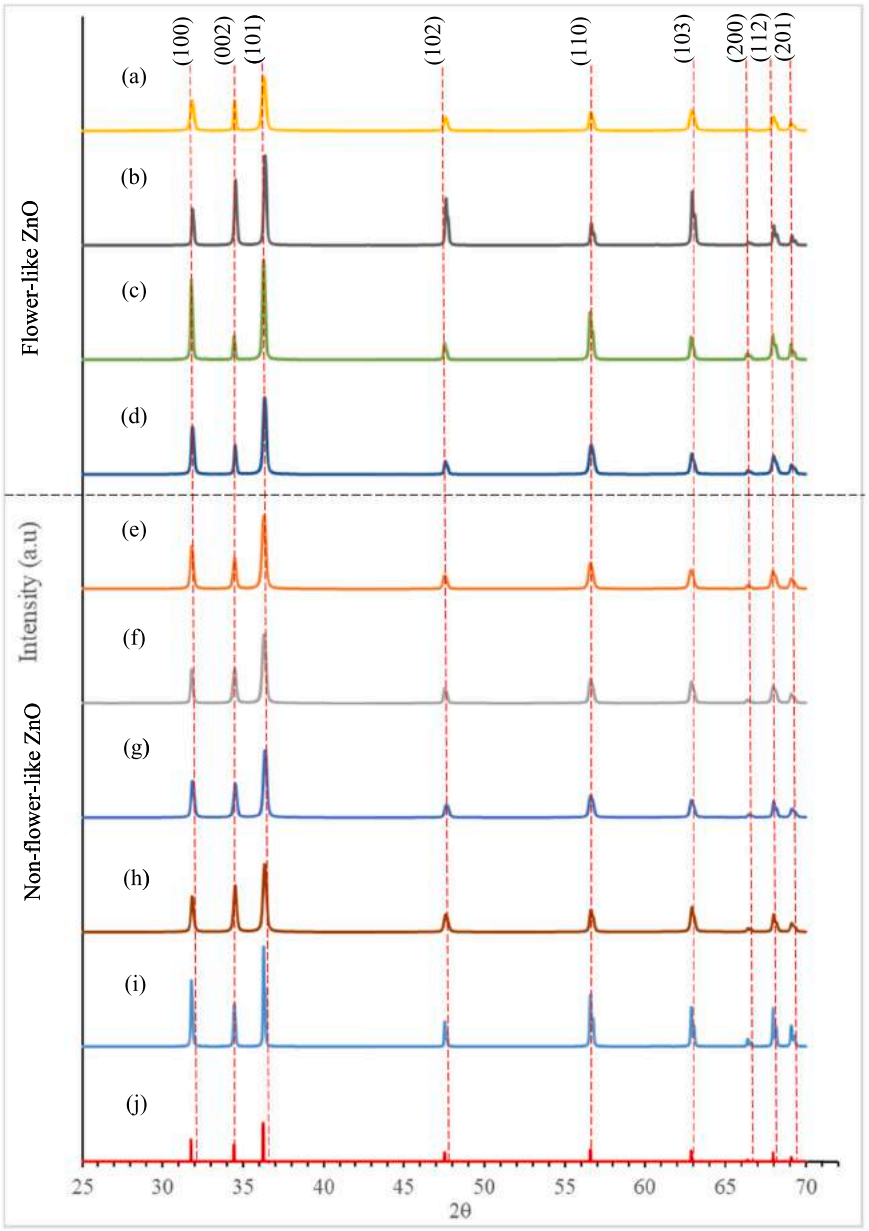

Fig. 2. XRD patterns of flower-like ZnO (a) flakes, (b) clusters, (c) rods, (d) needles; non-flower-like ZnO (e) nanoballs, (f) short-nanorods, (g) nanocubes, (h) nanoporous; (i) commercial ZnO; and (j) standard ZnO peak.

Table 2
Crystallite size of ZnO samples.

Samples	Crystallite size (nm)
Flower-like ZnO flakes	4.90 ± 1.5
Flower-like ZnO cluster	6.96 ± 2.25
Flower-like ZnO rods	7.30 ± 2.0
Flower-like ZnO needles	5.46 ± 1.05
ZnO nanoball	4.21 ± 1.0
ZnO short nanorods	5.08 ± 1.25
ZnO nanocubes	4.27 ± 1.5
ZnO nanoporous	4.63 ± 1.05
Commercial ZnO	10.51 ± 2.5

crystallite size indicating lower or equal to the grain size with the smallest particles. However, the crystallite and particle sizes were not the same possibly due to different grain sizes.

3.1.2. FESEM analysis of synthesized ZnO

3.1.2.1. Flower-like ZnO. Fig. 3 displays the formation of flower-like ZnO in the shape of flakes, clusters, rods, and needles as analyzed by FESEM. Various flower-like shapes were obtained by appropriate adjustment of pH and process temperature as well as change of chemical precursor. For instance, the formation of flower-like flakes occurred stemming from the reaction between $Zn(C_2H_3O_2)_2{\bullet}2H_2O$ and HMTA at pH 12 and a temperature of 150 °C for 3 h via the hydrothermal method. From the micrograph depicted in Fig. 3(a), the particles have thin and flat surfaces with thicknesses from 20 to 30 nm and lengths ranging from 70 to 120 nm. By increasing the pH and temperature of the process, flake shape was formed in the aggregates, thus forming a flower-like structure. The formation of the structure can be explained by the following equations:

$$(CH_2)_6N_4 + 6H_2O \leftrightarrow 6HCHO + 4NH_3 \quad (5)$$

$$NH_3 + H_2O \leftrightarrow NH_4^+ + OH^- \quad (6)$$

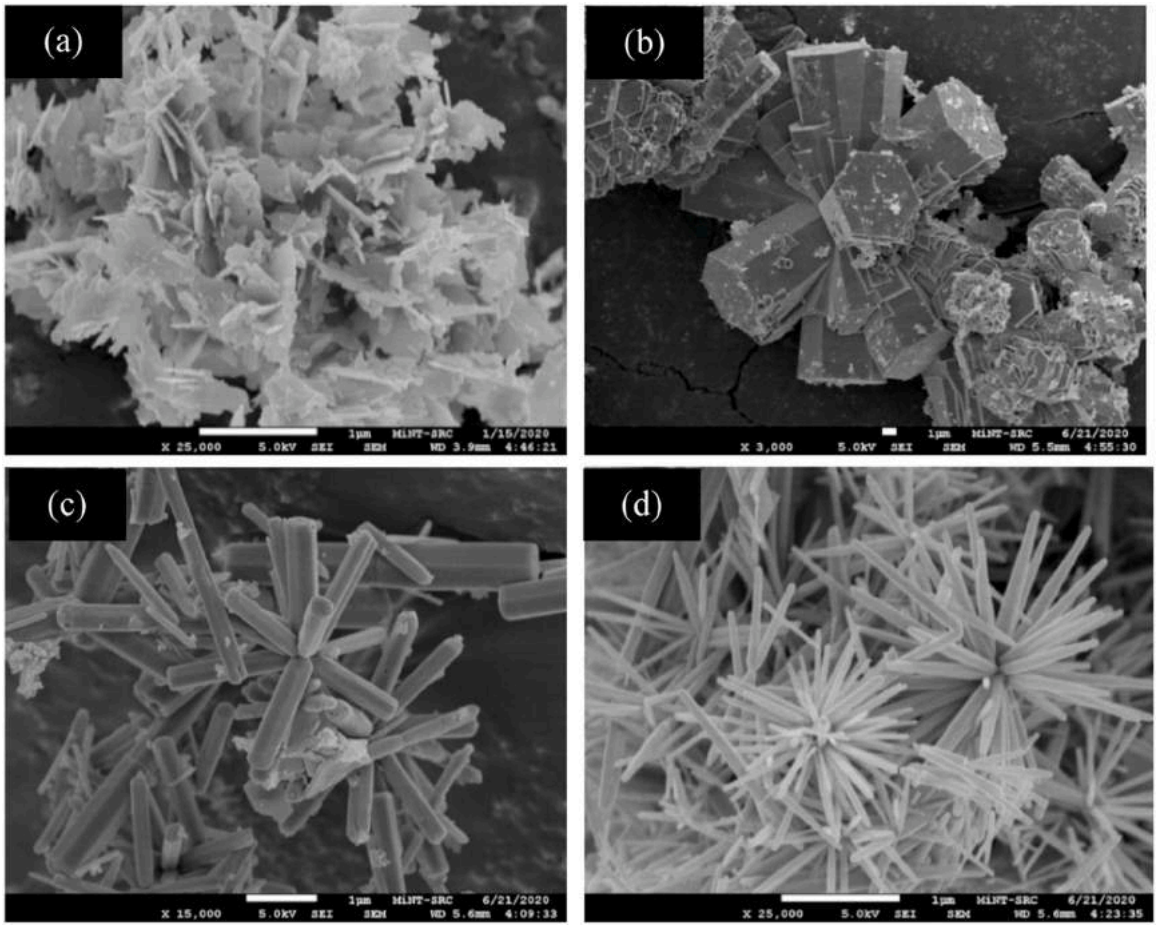

Fig. 3. FESEM images of flower-like ZnO: (a) flakes, (b) clusters, (c) rods, (d) needles.

$$Zn^{2+} + 2OH \leftrightarrow Zn(OH)_2 \quad (7)$$

$$Zn(OH)_2 + 2OH^- \text{ (from NaOH)} \rightarrow Zn(OH)_4^{2-} \quad (8)$$

$$Zn(OH)_4^{2-} \rightarrow ZnO + H_2O + 2OH^- \quad (9)$$

Furthermore, under hydrothermal conditions at the highest temperature (150 °C), Zn(C2H3O2)2•2H2O and HMTA as the reactants were rapidly hydrolyzed, where seven moles of the reactants produced ten moles of the products as shown in Eq. (5). As the reaction temperature increases, it accelerates the hydrolysis of HMTA and pushes the equilibrium forward which can be attributed to an increase in entropy [22,23]. As a result, the concentrations of Zn^{2+} and OH^- increased and formed zinc hydroxyl ions, consisting of a stacked layer of intercalated anions and a layer of water, and these layered structures eventually grow to form a flake-like morphology [31]. In addition, when the degree of supersaturation exceeded its critical value, a large quantity of ZnO nuclei were formed and aggregated. However, the highest pH (pH 12) contributed to the highest nucleation rate and formation of flake structure without the desired orientation [32]. Moreover, the highest pH could also contribute to the occurrence of more aggregation between the flakes [33], and thus form a flower-like structure.

In contrast, the formation of flower-like clusters (Fig. 3(b)) occurred when the sources of Zn^{2+} reagents were changed to Zn $(NO_3)_2$•$6H_2O$ and reacted with HMTA at 100 °C for 5 h. It was observed that the cluster-rod particles have lengths in the range of 4–6 µm and diameters in the range of 2–6 µm, thus forming large-sized rods with branched structures and aggregated to each other to form clusters. During the cluster formation process, the growth process of ZnO crystalline grains is generally divided into two parts, namely nucleation, and growth. With increasing temperature, Zn $(NO_3)_2$•$6H_2O$ and HMTA as reactants are rapidly hydrolyzed under hydrothermal conditions and increase the concentrations of Zn^{2+} and OH^-. The supersaturation conditions of Zn^{2+} and OH^- may lead to rapid nucleation to form ZnO nuclei [34]. For the highest concentration of HMTA, ammonia is highly formed and hydrolyzed to NH_4^+ and OH^-. The reaction between Zn^{2+} and OH^- forms ZnO nuclei and leads to the growth of ZnO rods along the c-axis [35]. After that, the other part of Zn^{2+} reacts with ammonia to produce a complex ion, $[Zn(NH_3)_4]^{2+}$. The complex ion is adsorbed on the surface of ZnO nuclei and reacts with excess OH^-. Therefore, the branch-structures are formed [36]. Nevertheless, the highest concentration of HMTA also contributes to excess OH^-, thus branched ZnO rods are formed in larger sizes and thicker [23]. Moreover, excessive number of OH^- may also contribute to more aggregation between branched ZnO rods and form large flower-like clusters. Equations for the formation of structure for flower-like clusters are provided in Appendix.

Furthermore, flower-like rods were successfully synthesized via the CBD method at 90 °C for 1 h through the reaction between Zn $(C_2H_3O_2)_2$•$2H_2O$ and HMTA. The formation of flower-like rods is depicted in Fig. 3(c). From the observations, the rod particles have lengths in the range of 1–2 µm and diameters in the range of 0.3–0.4 µm. These findings revealed that the application of the CBD method at lower temperatures induced the formation of flower-like rod structures in uniform size distribution and assembled leading to branch-like formation. The growth process mechanism of the crystalline grains for the flower-like rods was the same as that of flower-

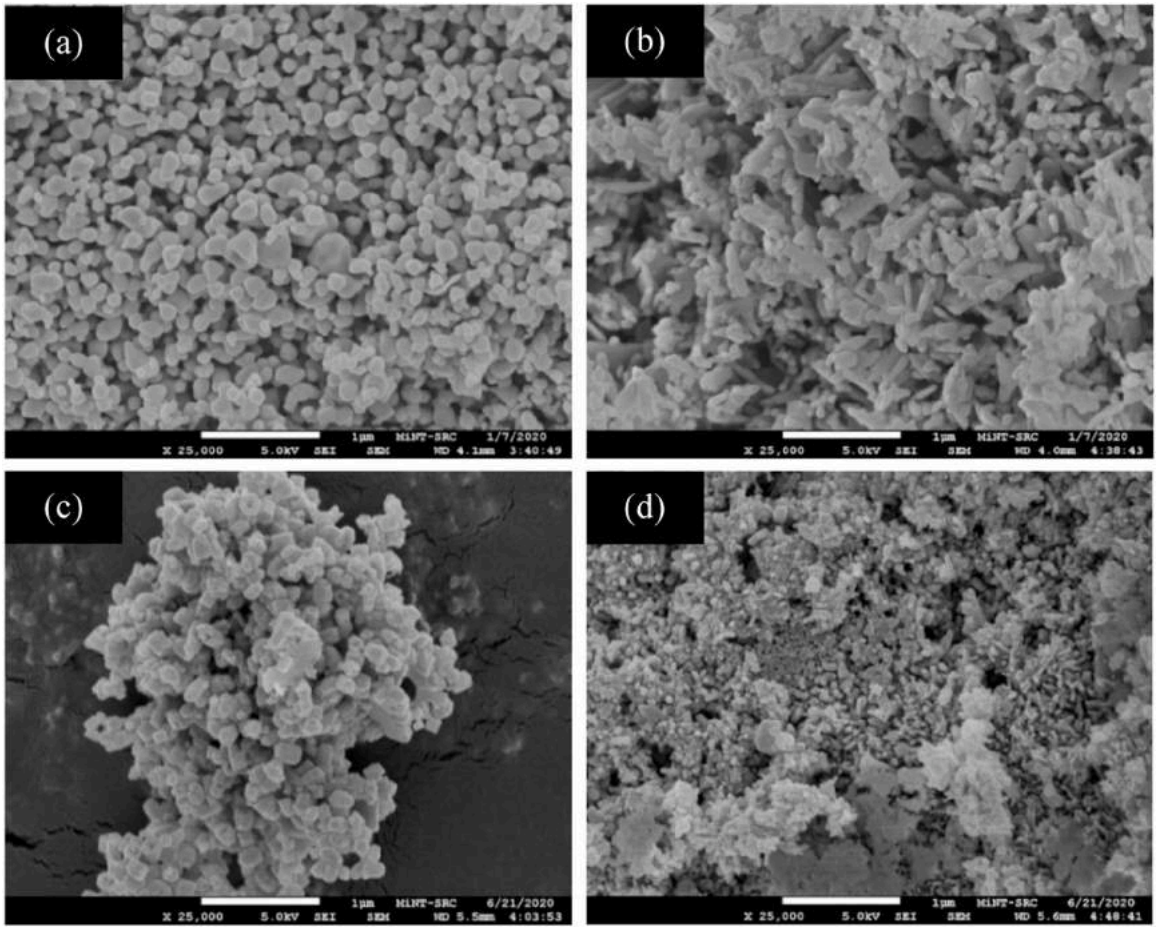

Fig. 4. FESEM images of non-flower-like ZnO: (a) nanoballs, (b) short-nanorods, (c) nanocubes, (d) nanoporous.

like clusters. With the aid of stirring, the particles are arranged and assembled, and slowly grow due to the energy acquired from stirring, thus forming flower-like rods [37]. Using CBD method, the reaction between $Zn(NO_3)_2$•$6H_2O$ and HMTA at 90 °C for 1 h resulted in the formation of flower-like needles as shown in Fig. 3(d). The needle particles have lengths in the range of 400–600 nm and diameters in the range of 30–60 nm. By changing the chemical precursor, the needle structure was formed uniformly in size distribution and assembled, resulting in branch-like formation. The growth process of ZnO crystalline grains for flower-like needles was also similar to that of flower-like clusters and rods. However, the formation of needle particles was small and thin due to less generation of OH^- under acidic conditions (pH 6) [33]. Equations for the formation of structure for flower-like rods and needles are provided in Appendix.

3.1.2.2. Non-flower-like ZnO. Fig. 4 displays the morphological variation of non-flower-like ZnO as analyzed using FESEM. Using the hydrothermal method, ZnO nanoballs were synthesized at pH 11 and 100 °C for 3 h through a reaction between $Zn(C_2H_3O_2)_2$•$2H_2O$ and NaOH. It was observed that the size distribution of nanoballs was uniform with diameters in the range of 100–200 nm and less agglomerated with each other. This formation could be explained by the source of Zn in the forms of $Zn(OH)_2$ precipitates and $Zn(OH)_4^{2-}$ species according to the stoichiometric ratio of Zn^{2+} on OH^- [38]. The $Zn(OH)_2$ precipitates under hydrothermal conditions were considerably dissolved to form Zn^{2+} and OH^- ions. If the products of Zn^{2+} and OH^- exceed the critical value, nanoballs will precipitate from the solution [39]. The solubility of ZnO was significantly smaller than that of $Zn(OH)_2$ under hydrothermal conditions, which caused $Zn(OH)_2$ precipitates to strongly transform into nanoballs based on the following reactions:

$$Zn(OH)_2 \rightarrow Zn^{2+} + 2OH^- \quad (31)$$

$$Zn^{2+} + 2OH^- \rightarrow ZnO + H_2O \quad (32)$$

In the initial stage of the process, the concentrations of Zn^{2+} and OH^- were relatively higher so that the growth of nanoparticles in different directions was considerable. When the concentrations of Zn^{2+} and OH^- reach the ZnO supersaturation level, ZnO begins to nucleate and completely grow [40].

Meanwhile, Fig. 4(b) portrays the morphology of short-nanorods observed using FESEM. which were hydrothermally synthesized at pH 11 and 100 °C for 3 h through the reaction between Zn $(C_2H_3O_2)_2$•$2H_2O$ and HMTA. The particles of short-nanorods have lengths in the range of 10–400 nm and diameters in the range of 30–100 nm. By changing the OH^- reagent sources, the morphology of ZnO varied. The short-nanorod growth process was also similar to that of flower-like rods, which was generally divided into two parts, namely nucleation, and growth. However, it was observed that the short-nanorod particles formed were agglomerated with each other and not uniform in size distribution which may be due to the short period of hydrothermal process. Consequently, the particles were not completely grown into rod structures.

On the other hand, ZnO nanocubes were successfully synthesized via hydrothermal method at pH 11 and 100 °C for 10 h through the reaction between Zn(C2H3O2)2•2H2O and HMTA. The formation of nanocubes is depicted in Fig. 4(c). The effect of reaction time was

Table 3
Particle size distributions of synthesized ZnO.

Type of ZnO	Morphology of ZnO	Particle size		
		Length	Diameter	Thickness
Flower-like	Flakes	70–120 nm	–	20–30 nm
	Clusters	4–6 µm	2–6 µm	–
	Rods	1–2 µm	0.3–0.4 µm	–
	Needles	400–600 nm	30–60 nm	–
Non-flower-like	Nanoballs	–	100–200 nm	–
	Short-nanorods	10–400 nm	30–100 nm	–
	Nanocubes	100–200 nm	30–100 nm	–
	Nanoporous	–	100–400 nm	–
Commercial ZnO		40–700 nm	30–400 nm	–

taken into account during the formation of nanocubes. Apparently, the particles have lengths in the range of 100–200 nm and diameters in the range of 30–100 nm. As the period of the hydrothermal process was extended, the nanocube structures were formed with a slightly uniform size distribution and less agglomeration. Since the chemical precursor and method for nanocubes preparation were similar to that of short-nanorods, the growth mechanism was the same where the process was divided into nucleation and growth. However, the particles became slightly shorter with a prolonged growth time exceeding 10 h. As a result, the growth rate decreased and finally ceased due to insufficient supply of Zn^{2+} and OH^- ions. Thus, the length of the growing rod structure became shorter, resulting in the formation of nanocubes.

In Fig. 4(d), the formation of nanoporous was observed from the reaction between $Zn(C_2H_3O_2)_2{\bullet}2H_2O$ and HMTA via the hydrothermal method at 100 °C for 5 h. From the micrograph, nanoporous have diameters ranging from 100 to 600 nm. It was verified that changes in the concentrations of chemical precursor induced the formation of nanoporous, where the particles strongly agglomerated with each other. Similar to previous ZnO morphological variation, the increase in temperature caused the reactants to hydrolyze rapidly under hydrothermal conditions and then increased the concentrations of Zn^{2+} and OH^-. However, high concentration of HMTA used (1 M) would not adhere to the growth direction of ZnO as it has no preferred direction and then transformed into spherical nanoparticles. Moreover, the excessive number of OH^- produced from HMTA has resulted in more aggregation between particles [25]. Equations for the formation of non-flower-like structures are provided in the Appendix.

3.1.2.3. Commercial ZnO. Fig. 5 displays the morphology of commercial ZnO. From the observation, it showed that commercial

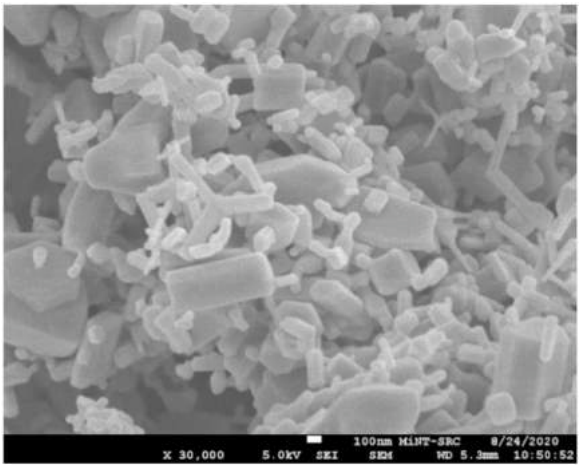

Fig. 5. FESEM images of commercial ZnO.

ZnO has nanorod morphology with a mixture of smaller and larger nanorod sizes. The nanorods particles have lengths in the range of 40–100 nm and diameters in the range of 30–60 nm for smaller nanorods, while larger nanorods have lengths in the range of 300–700 nm and diameters in the range of 100–400 nm. Since commercial ZnO was purchased from the manufacturer, further explanation is not included in this study.

From the overall findings, the ascending order of particle sizes for all ZnO structure types could be arranged as nanoball < nanoporous < nanocubes < flower-like flakes < short-nanorods < flower-like needles < commercial < flower-like rods < flower-like cluster. It was evidenced that morphological variation of ZnO in terms of shape, structure, and size could occur by changing preparation methods and conditions. The hydrothermal method was found to produce a better uniformity of ZnO particle size distribution compared to the CBD method. Moreover, different chemical precursors used could also vary the ZnO morphology. When the main sources of OH^- are originated from HMTA, it results in various structure morphologies, and when OH^- is originated from NaOH, it results in oval-like nanostructures. This may be influenced by long-chain HMTA polymers and nonpolar chelating agents that prefer to attach to the non-polar facets of the zincite crystal, thereby cutting off Zn^{2+} ions access to them leaving only the polar (001) face for epitaxial growth [23]. Thus, HMTA acts more like a shape-inducing polymer surfactant that can control the morphology of ZnO than to supply hydroxyl ions. Table 3 summarizes the particle size distributions of synthesized ZnO with different morphologies.

Furthermore, when the pH condition is higher during the growth process, it may induce the particles to become more aggregated with each other [41]. In fact, by prolonging the processing period, it could decrease the growth rate and then cease due to insufficient supply of Zn^{2+} and OH^- ions, resulting in a shorter structure of ZnO [38]. Moreover, the advantage of applying higher temperatures during the growth process could increase the reaction rate and contribute to higher production of ZnO particles compared to lower temperatures [42]. Thus, it can be inferred that the CBD method could synthesize flower-like morphology in a 3-dimensional structure better than the hydrothermal method. The formation of flower-like rods and needles via the CBD method may be influenced by continuous stirring [33]. Meanwhile, flower-like clusters and flakes synthesized via the hydrothermal method were clustered and aggregated like flower structures.

3.1.3. FTIR analysis of synthesized ZnO

Fig. 6 depicts the FTIR spectra of the synthesized ZnO in the range of 600–4000 cm^{-1}. The Zn-O stretching and deformation vibration were detected at bands from 600 to 700 cm^{-1} for each ZnO structure. Generally, the absorption bands for metal oxides are below 1000 cm^{-1} stemming from inter-atomic vibrations [43]. The bands at 3200 – 3600 cm^{-1} corresponded to the O-H vibration mode due to the adsorption of water vapor from the surroundings and residual moisture during ZnO synthesis [29]. The changes of O-H peak

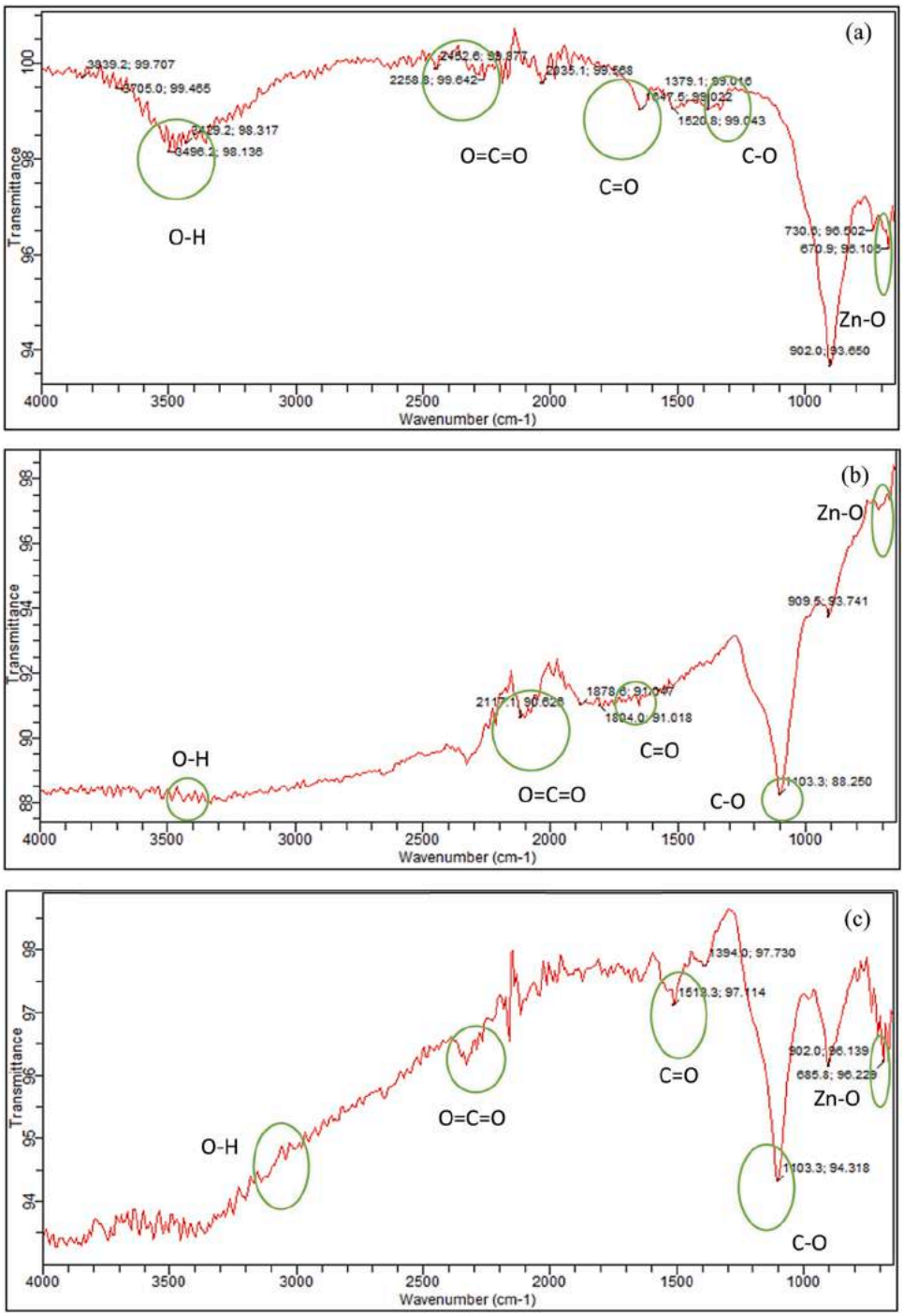

Fig. 6. FTIR spectrums of flower-like ZnO (a) flakes, (b) clusters, (c) rods, (d) needles; non-flower-like ZnO (e) nanoballs, (f) short-nanorods, (g) nanocubes, (h) nanoporous; and (i) commercial ZnO.

positions from sharp to broad could be attributed to the variation in pH conditions. This is supported by Wahab et al. [33], which also claimed that the structure formation is highly influenced by the movement of O-H peak. Moreover, the carboxyl group (C═O) was detected at bands from 1500 to 1600 cm^{-1}. The C═O stretching of Zn $(C_2H_3O_2)_2$•$2H_2O$ could be observed in all synthesized ZnO except for flower-like clusters and needles, similar to that reported by Thilagavathi & Geetha [44]. Meanwhile, the stretching mode of the C-O component was exhibited at bands from 1000 to 1300 cm^{-1}. Furthermore, CO_2 band (O═C═O) was detected at 2000 – 2500 cm^{-1} which could be due to oxidative decomposition of organic species [45]. Similarly, Pholnak et al. [46] also reported the presence of O═C═O in the range of 2000–2500 cm^{-1}. These results showed that all the synthesized ZnO have good functional groups and selective elements.

3.2. Desulfurization of thiophene

3.2.1. Characteristics of untreated thiophene solution

The performance of the synthesized ZnO was evaluated in the desulfurization of thiophene via a photocatalytic reactor under different conditions, including non-flower-like ZnO as it may have higher potential in enhancing the desulfurization of thiophene and could be a reference for future studies. Thiophene is the simplest

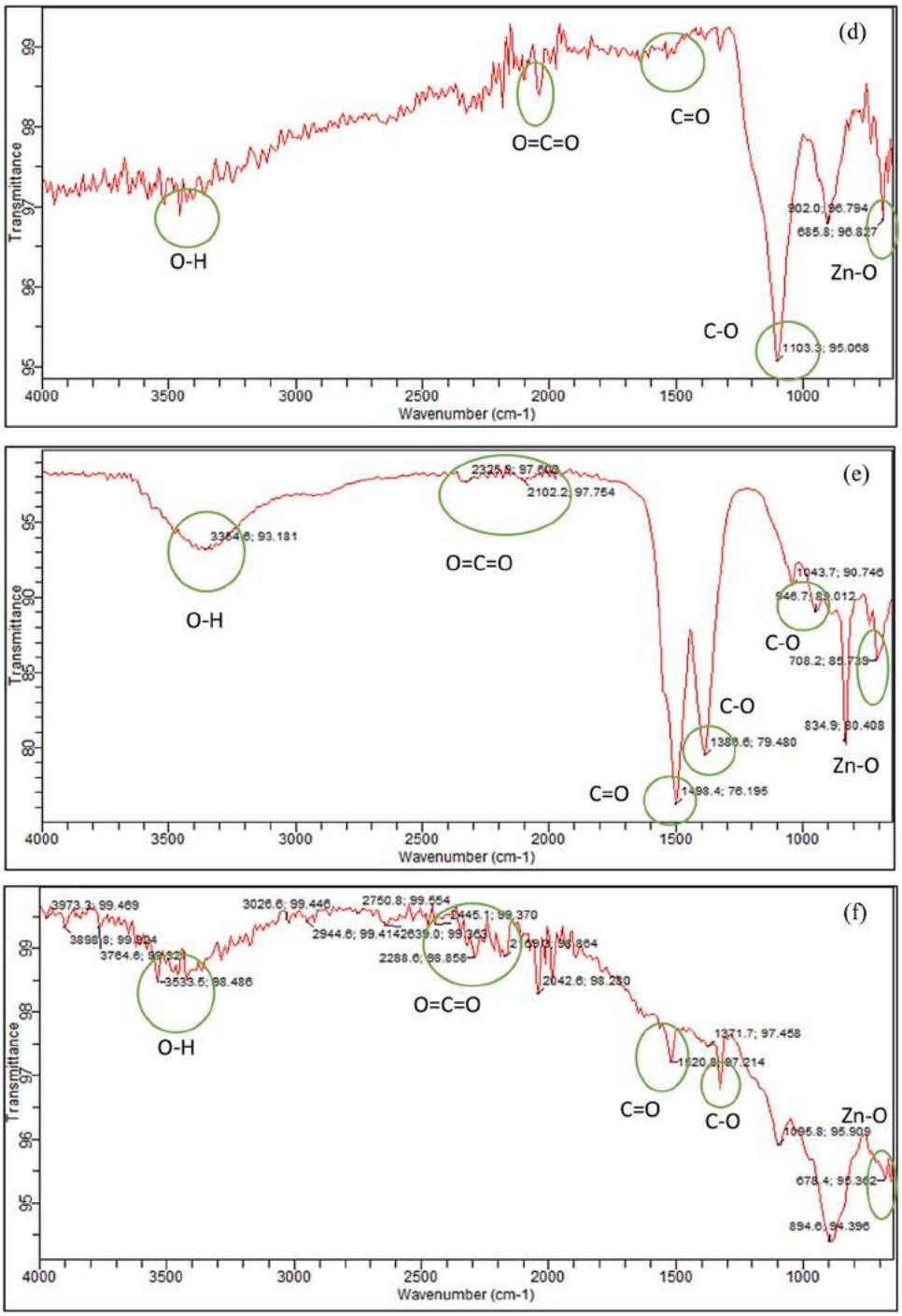

Fig. 6. (*continued*)

aromatic compound containing sulfur atoms with the formula C_4H_4S and belongs to the heterocyclic compounds [47]. It is a colorless liquid with a mild pleasant odor reminiscent of benzene as it shares some similar chemical properties. However, thiophene is categorized in sulfur-containing compounds (SCCs) and is known as an aromatic compound that has toxic and flammable behavior that can cause air pollution during combustion.

Table 4 shows the characteristics of thiophene solution before treatment. The initial concentration and pH were kept constant in this study to observe the performance of different ZnO morphologies as photocatalysts in the desulfurization of thiophene. Different initial turbidity values were obtained for each sample. This was probably due to the number and size of ZnO particles present in the solution as a foreign matter and then affecting the turbidity reading.

3.2.2. *Effect of different initial pH*

Primary studies were conducted to identify toptimum initial pH conditions. In this primary study, flower-like ZnO needles were employed for the desulfurization of thiophene under pH 6–8. According to Fan et al. [23], flower-like ZnO has higher photocatalytic degradation efficiency in degrading inorganic compounds due to the larger amount of oxygen vacancies on its surface which could act as an active center to prevent recombination of photoelectrons and photo-holes, thus increasing the photocatalytic

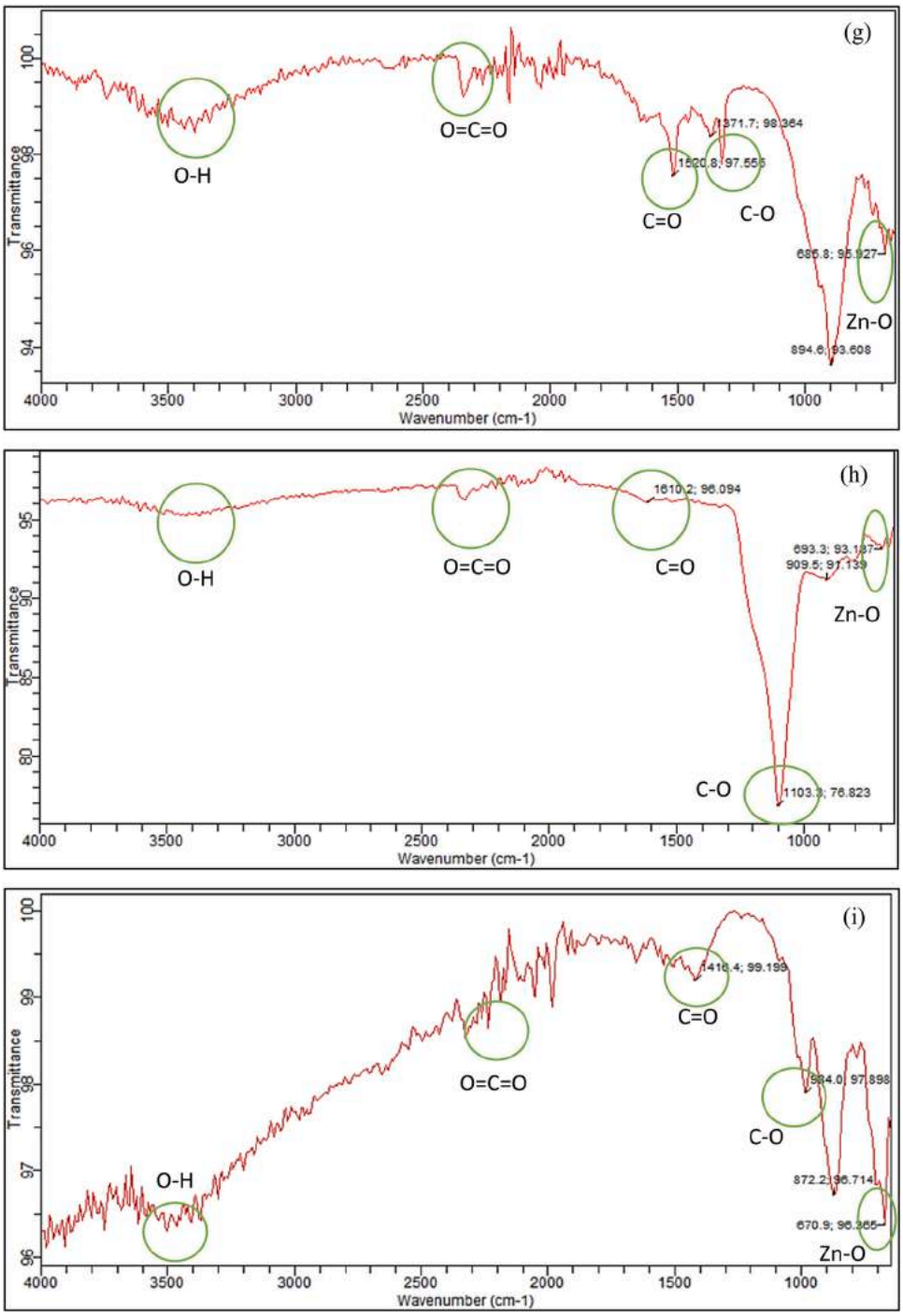

Fig. 6. (*continued*)

activities. Therefore, the use of flower-like ZnO needles is expected to induce higher photocatalytic degradation efficiency for the desulfurization of thiophene.

On the other hand, Fig. 7 shows the desulfurization of thiophene in the presence of 0.05 g/L flower-like ZnO needles at pH 6, 7, and 8. These pH conditions were selected as less acidic and alkaline conditions are harmless to humans and prevent machine damage. Based on the results obtained, the performance of thiophene desulfurization was the highest at pH 7 (23.55%) and 8 (23.90%) after 90 min. In another study conducted by Hamdan et al. [5], pH 7 was the optimum condition for photocatalytic degradation of thiophene using ZnO/fibrous nanosilica (KCC-1). In contrast, the performance of thiophene desulfurization was only 21.91% after 90 min at pH 6. For an in-depth study, the point of zero charge (pH_{zpc}) of the catalyst could be used to consider the optimum pH for the reaction [48]. A previous study has reported that the pH_{zpc} for ZnO is 8.19 [45]. In this study, the pH_{zpc} for flower-like ZnO needles was 8.19. This may be due to the synthesized flower-like ZnO needles having only selective compound, corresponding to the wurtzite structure and no impurities detected.

Furthermore, if the pH_{zpc} of the catalyst is higher than the pH of the solution, the catalyst surface is positively charged, and if the pH_{zpc} of the catalyst is lower than the pH of the solution, the catalyst surface is negatively charged [48]. For pH 7 and 8, the surface of the ZnO needles was considered positively charged as pH_{zpc} was higher than the pH of the solution. The results revealed that the

Table 4
Characteristics of untreated thiophene solution.

Thiophene parameters	Reading
Initial concentration	300 ppm
Initial pH	7
Initial turbidity (NTU)	
Flower-like ZnO flakes	10.34 ± 4.09
Flower-like ZnO cluster	7.9 ± 4.0
Flower-like ZnO rods	1.73 ± 4.09
Flower-like ZnO needles	4.75 ± 3.04
Non-flower-like ZnO nanoball	8.83 ± 3.50
Non-flower-like ZnO short-nanorods	9.2 ± 3.80
Non-flower-like ZnO nanocubes	12.10 ± 4.09
Non-flower-like ZnO nanoporous	11.33 ± 3.04
Commercial ZnO	7.82 ± 4.09

enforcement of the reaction in alkaline conditions can be associated with an increase in hydroxyl ions that induce more hydroxyl radical formations. Hydroxyl radical (•OH) is the main oxidizing agent that plays an important role in the degradation of thiophene and organic compounds into carbon dioxide (CO_2) and water (H_2O) [49]. Thus, it can be concluded that the desulfurization of thiophene is more appropriate in neutral and alkaline conditions than in acidic conditions. However, at pH 8, higher desulfurization was achieved only after 60 min compared to pH 7 which achieved the highest desulfurization after 20 min. Furthermore, pH 7 was preferred due to its neutral condition, safer and less damage to the machines. Therefore, pH 7 was applied as the initial pH condition, and followed by photocatalyst loading of 0.05 g/L to further evaluate the performance of the synthesized ZnO photocatalysts for desulfurization of thiophene. Similar initial pH condition was also applied for the investigation of non-flower-like ZnO performance for desulfurization of thiophene as a reference for future studies.

3.2.3. Performance of synthesized ZnO for desulfurization of thiophene

Fig. 8 shows the performances of the synthesized ZnO photocatalysts for desulfurization of thiophene at pH 7 and 0.05 g/L loading. Based on the results, the performance of desulfurization using different ZnO morphologies could be arranged in descending order: flower-like flakes > nanocubes > nanoballs > flower-like clusters > nanoporous > commercial > short-nanorods > flower-like needles > flower-like rods. It was evidenced that the flower-like flakes indicated a higher performance of thiophene desulfurization of 29.87% after 90 min compared to flower-like rods (21.98%). This may be related to the effect of ZnO morphology on the degradation efficiency.

According to the FESEM analysis (Fig. 3), the flake shape has thin and flat surfaces. The flower-like flakes also have high purity without impurities based on XRD analysis (Fig. 2(a)), and also have a smaller crystallite size of 4.90 nm, indicating a smaller particle size. These characteristics are favorable in increasing the number of surface-active sites of ZnO and producing more hydroxyl radicals during irritation leading to higher performance of thiophene desulfurization [50]. Previous studies have also claimed that nanoflakes and flower-like morphology contribute to large surface areas and surface-active sites of photocatalyst, leading to higher degradation of thiophene [18].

The second-highest performance of thiophene desulfurization was demonstrated by ZnO nanocubes. The nanocube structure has high purity and no impurities were detected from the XRD analysis (Fig. 2(g)). Based on FESEM analysis (Fig. 9), ZnO nanocubes have cube structures, approaching uniform nano-sizes. However, the nanocubes agglomerated with each other probably due to a decrease in the number of surface-active sites of ZnO and thus affected the desulfurization efficiency. Compared with nanoballs with slightly larger size, the number of surface-active sites of nanoballs was lower than that of nanocubes. Although ZnO nanoparticles have the lowest crystallite size, the particle sizes are not necessarily the lowest. Different grain sizes are combined and agglomerated with each other and form slightly larger sized particles [30]. Thus, the particle size of ZnO nanoparticles was slightly larger than that of ZnO nanocubes, thus resulting in lower desulfurization for ZnO nanoballs than ZnO nanocubes which were 27.2% and 27.4%, respectively. Meanwhile, the desulfurization performances of flower-like clusters, nanoporous, commercial, short-nanorods, flower-like needles, and flower-like rods were 26.42%, 25.65%, 24.32%, 23.9%, 23.55%, and 21.98%, respectively, after 90 min

From the results obtained, it can be concluded that as the ZnO particle sizes increase, the number of surface-active site areas of the ZnO particles and thiophene desulfurization efficiency decreases [19]. In addition, agglomeration of ZnO particles can also affect the lower number of surface-active sites available for photocatalytic

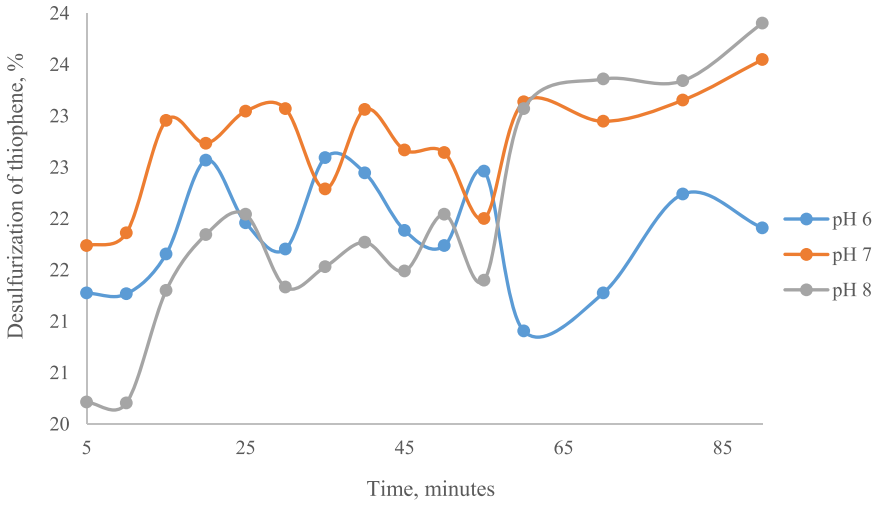

Fig. 7. Desulfurization of thiophene in the presence of flower-like ZnO needles at different pH.

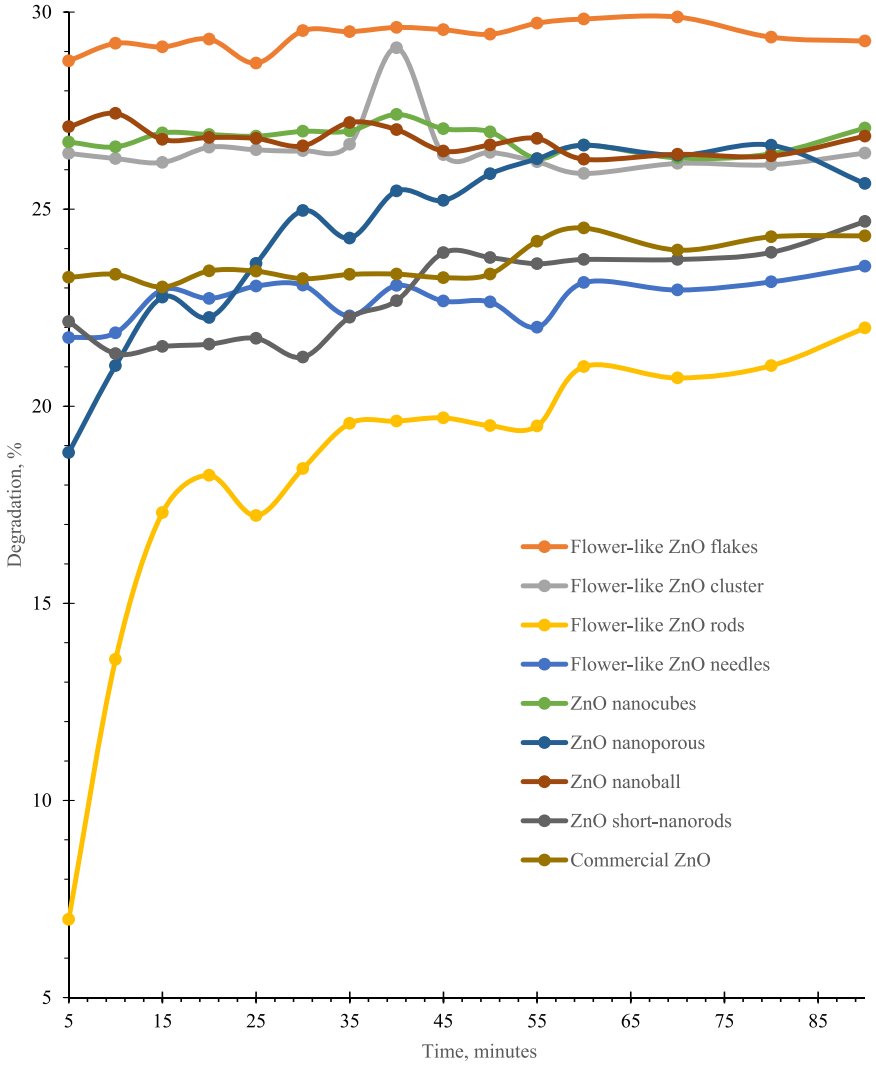

Fig. 8. Performance of the synthesized ZnO for desulfurization of thiophene at pH 7 for 90 min.

degradation and deactivation of activated molecules due to collisions of activated molecules with ground-state molecules [6]. This resulted in a decline in desulfurization efficiency. Moreover, it can also be concluded that ZnO particles with larger sizes and more agglomerates could reduce the availability of surface-active sites of the particles for the reaction to occur. As a result, less hydroxyl radicals were produced from the irradiated photocatalyst and led to low thiophene desulfurization.

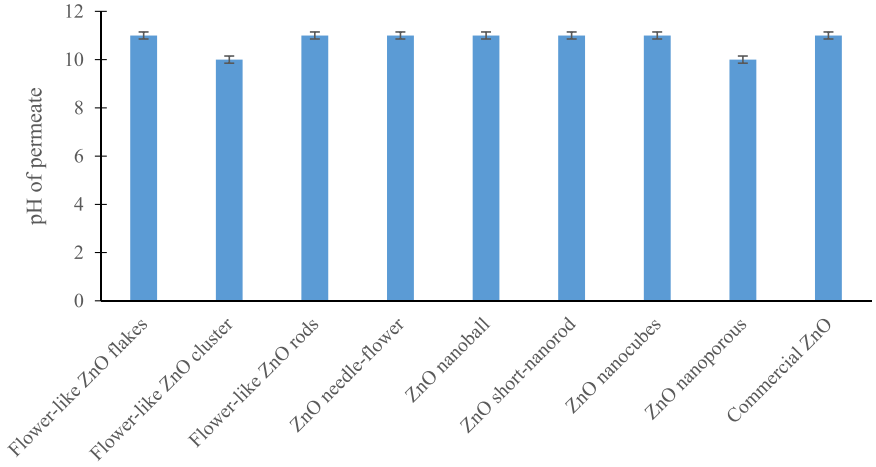

Fig. 9. pH of permeate after desulfurization using different ZnO morphologies.

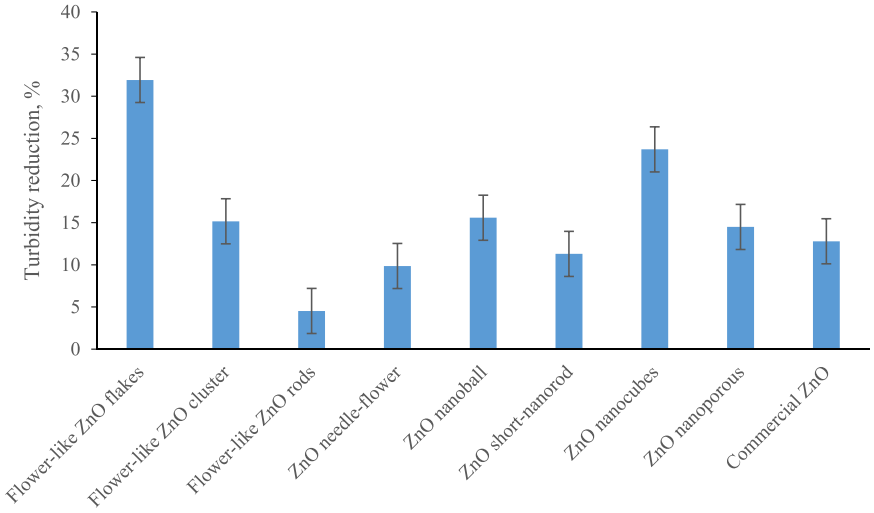

Fig. 10. Turbidity of permeate after treatment using different ZnO morphologies.

3.3. Permeate analysis

3.3.1. pH analysis

Fig. 9 shows the pH of permeate after treatment using different ZnO morphologies as photocatalysts. The initial pH of the thiophene solution was fixed at 7 for all samples. From the results, it can be observed that the pH of the permeate increased after treatment. This could be due to an increase in the production hydroxyl radical during desulfurization and leads to a higher number of OH^- ions present in the solution, thus increasing the pH [6,36]. According to Hamdan et al. [5], neutral conditions could desulfurize thiophene better than acidic conditions. The enforcement of reaction in neutral conditions could increase the formation of hydroxyl radicals that act as oxidizing agents in the desulfurization of thiophene. Meanwhile, the morphology of flower-like flakes could increase the surface-active site of the photocatalyst when more hydroxyl radicals are formed and induce efficient desulfurization [50].

3.3.2. Turbidity analysis

Fig. 10 shows the turbidity reduction of thiophene solution after 90 min of desulfurization using different ZnO morphologies as photocatalysts. The results revealed that the flower-like flakes had the highest turbidity reduction than others which was 31.93%. This could be attributed to the large amount of thiophene compounds in solution being converted to degraded compounds [49]. Meanwhile, the lowest turbidity reduction was obtained by flower-like rods of 4.52%, indicating that a small amount of thiophene compounds were degraded. Undegraded thiophene compounds may contribute to the highest turbidity readings [51]. Hamdan et al. [5] also agreed that desulfurization of thiophene in neutral conditions results in higher turbidity reduction. As noted earlier, the formation of oxidizing agents is greater in neutral conditions. Meanwhile, the flower-like flake morphology may increase the surface active-site leading to higher desulfurization of thiophene and higher turbidity reduction [50].

3.4. Kinetics of photo-desulfurization

The kinetics of thiophene desulfurization were studied and analyzed based on pseudo-first-order and pseudo-second-order models. This study was conducted to evaluate the efficiency of synthesized ZnO photocatalysts in thiophene desulfurization. In this study, two kinetic models were developed based on experimental data to investigate their applicability. From the experimental results, the concentration equilibrium (C_e) values were 877.89, 792.67, 659.53, 706.46, 805.51, 740.55, 811.69, 769.45, 729.68 mg/g for flower-like flakes, flower-like clusters, flower-like rods, flower-like needles, nanoballs, short-nanorods, nanocubes, nanoporous and commercial ZnO, respectively. Table 5 shows that the pseudo-first-

Table 5
Kinetic parameters of different ZnO morphologies for desulfurization of thiophene.

Sample	Pseudo-first-order				Pseudo-second-order	
	R^2	K (min^{-1})	C_e (mg/g)	R^2	K (g/mgmin^{-1})	C_e (mg/g)
Flower-like ZnO flakes	0.080	-0.036	4.06	0.9997	0.0011	909.09
Flower-like ZnO clusters	0.357	-0.028	1.23	0.9983	0.0013	769.23
Flower-like ZnO rods	0.860	0.031	295.66	0.9945	0.0014	714.29
Flower-like ZnO needles	0.215	0.011	35.20	0.9987	0.0014	714.29
ZnO nanoball	0.517	-0.035	1.10	0.9997	0.0013	769.23
ZnO short-nanorod	0.752	0.023	127.21	0.9977	0.0013	769.23
ZnO nanocubes	0.073	-0.013	3.74	0.9994	0.0013	769.23
ZnO nanoporous	0.837	0.079	333.25	0.9981	0.0012	833.33
Commercial ZnO	0.564	0.037	72.05	0.9991	0.0014	714.29

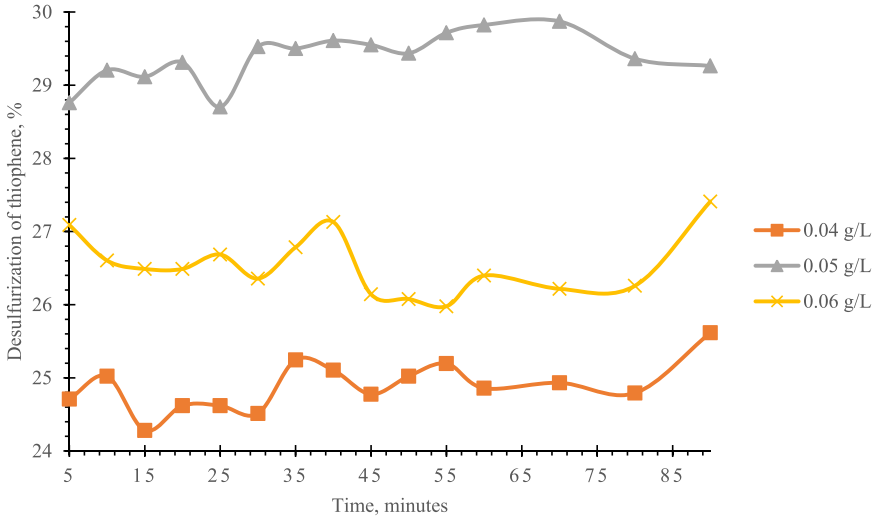

Fig. 11. Desulfurization of thiophene at different loadings of flower-like ZnO flakes photocatalyst.

order kinetic models have the lowest linear regression (R^2) values which proved that the models were unsuitable and inapplicable. However, the R^2 values of pseudo-second-order kinetic models were the highest, which proved that these models were applicable for desulfurization of thiophene, suggesting that the desulfurization of thiophene may follow chemisorption [52].

Chemisorption occurs when thiophene molecules are held on the surface of ZnO by chemical forces as short covalent chemical bonding through electron sharing [53]. Thus, the proposed photocatalytic degradation mechanism of thiophene is in agreement with the chemisorption mechanism, where the reaction between the hole, h^+_{vb} (from ZnO), and OH^- (from thiophene) formed highly reactive hydroxyl radicals leading to degradation of thiophene compounds. Moreover, the reaction between electron, e^-_{cb} (from photoexcitation in ZnO), and oxygen present also contributed to the formation of hydroxyl radicals for degradation of thiophene.

Furthermore, the C_e values calculated for the pseudo-second-order are also in agreement with the experimental data of degradation efficiency. From Table 4, the flower-like flakes had the highest C_e values, suggesting that thiophene was highly desulfurized after 90 min of treatment. According to collision theory, the greater the surface-active site of flower-like ZnO flakes, the more hydroxyl radicals could be produced, thus inducing a greater chance for oxidative reaction to occur.

According to Hairom et al. [14], the reaction between the holes (h^+_{vb}) in the valence band (ZnO photocatalyst) and OH^- (thiophene solution) will produce hydroxyl radicals and lead to the degradation of thiophene compounds. When the photocatalyst has greater surface-active sites, the reaction between the hole and OH^- will be greater and faster, and then increase the number of hydroxyl radicals and the degradation of bonds in thiophene per period. Moreover, Alhaddad & Shawky [50] proved that flower-like and flake structures could improve the surface-active site and light absorption. The flake shape increases the light absorption as the number of electrons (e^-_{cb}) generated is greater. Thus, the reaction between e^-_{cb} with oxygen molecules produced more hydroxyl radicals leading to higher degradation of thiophene per period in this study.

3.5. Optimum conditions of flower-like ZnO flakes for desulfurization of thiophene

3.5.1. Effect of different photocatalyst loadings

Owing to the highest potential in desulfurization of thiophene, the optimum conditions of flower-like ZnO flakes were determined based on photocatalyst loading and treatment period. The effect of temperature on desulfurization of thiophene was not considered in this study. Desulfurization was conducted at room temperature for the purpose of reducing costs by limiting the use of high temperature conditions. Fig. 11 shows the effect of different loadings of flower-like ZnO flakes for desulfurization of thiophene. It was found that 0.05 g/L was the optimum photocatalyst loading for desulfurization of thiophene as it achieved the highest desulfurization of 29.87%, followed by 0.06 g/L (27.41%) and 0.04 g/L (25.62%) loading. Hamdan et al. [54] in their study also reported that 0.05 g/L was the optimum photocatalyst loading of ZnO/KCC-1 to degrade 300 ppm synthetic thiophene concentration. Generally, if the photocatalyst dosage increases, the thiophene desulfurization rate will increase due to the increment of active sites, and more hydroxyl radicals are produced from irradiation of flower-like ZnO flakes in large amounts [38]. At lower photocatalyst loading, desulfurization of thiophene is low as more light is transmitted through the reactor, and only lower transmitted radiation will be utilized in the photocatalytic reaction [55]. However, beyond the optimum loading, the degradation rate may be reduced due to increased suspension opacity, and thus increase light scattering, reduce photon infiltration depth and less photocatalyst can be activated [51]. Hamdan et al. [5] agreed that 0.05 g/L is an efficient photocatalyst loading, especially for ZnO-KCC-1 which provides the best desulfurization of thiophene. Therefore, it can be inferred that flower-like ZnO flakes with a loading of 0.05 g/L favorably induce the highest desulfurization of thiophene and could yield the best permeate quality.

3.5.2. Effect of contact time

Fig. 12 depicts the effect of contact time on the performance of flower-like ZnO flakes photocatalyst for desulfurization of thiophene. From the graph, it showed that 90 min was the optimum time taken for thiophene to be desulfurized. Beyond that, desulfurization efficiency declined drastically. Typically, reaction rates decrease with time as reactant concentrations decrease when converted into products [56]. Deceleration of thiophene degradation rate after 90 min could be due to insufficient hydroxyl radicals produced during irritation of ZnO flakes when the maximum limit of photon absorption in the reactor has been reached [18]. Moreover, kinetic studies proved that the adsorption reached equilibrium at 90 min. Further treatment will not result in desulfurization and its performance will decline. After reaching equilibrium, the migration of solute species from the solution ceases [57]. Thus, the most favorable contact time

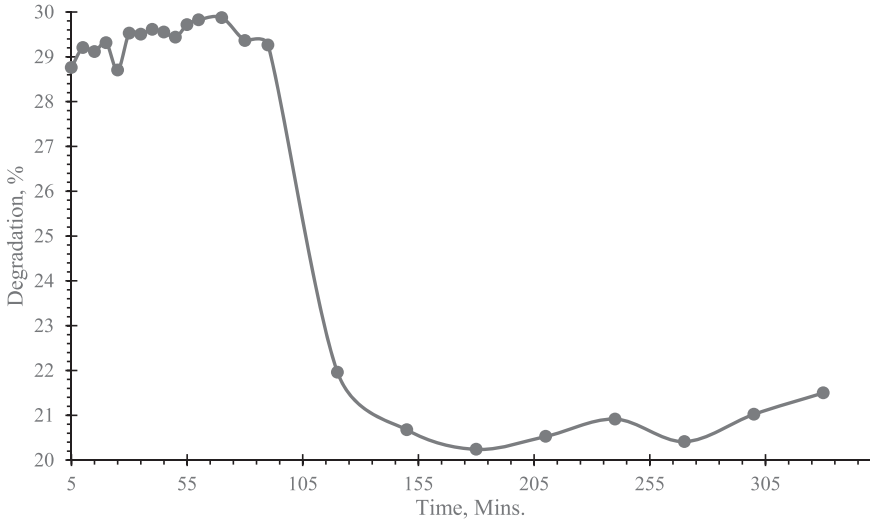

Fig. 12. Desulfurization of thiophene in the presence of flower-like ZnO flakes after 5 h.

for desulfurization of thiophene using flower-like ZnO flakes is 90 min

4. Conclusion

From the results obtained, it can be concluded that flower-like and non-flower-like ZnO were successfully synthesized via hydrothermal and CBD methods. Flower-like ZnO photocatalysts were in the shapes of flakes, clusters, rods, and needles. For non-flower-like ZnO, the photocatalysts were in the shapes of nanoballs, short-nanorods, nanocubes, and nanoporous. Based on the physicochemical properties, the XRD patterns confirmed that all ZnO morphologies have standard wurtzite structure, good crystallinity, and no impurities. The FESEM results showed that the average particle size of the flower-like ZnO synthesized was 700 nm and 400 nm for non-flower-like. In addition, FTIR analysis also confirmed that all ZnO morphologies contained appropriate functional groups at particular bands. For the performance of thiophene desulfurization, the results confirmed that flower-like ZnO flakes demonstrated the best photocatalyst performance among others owing to their thin and flaky structures which increased the number of surface-active sites and improved light absorption to yield more hydroxyl radicals during irradiation to degrade thiophene compounds. Higher pH and turbidity reduction of the permeate confirmed that the thiophene compounds in solution were highly degraded after treatment. In this study, it was observed that the kinetics of photo-desulfurization of thiophene fitted well with pseudo-second-order models. This study proved that flower-like ZnO flakes have the highest desulfurization rate due to their morphological characteristics. Furthermore, optimum conditions for thiophene desulfurization in the presence of flower-like ZnO flakes as photocatalyst were pH 7, 0.05 g/L photocatalyst loading, and 90 min contact time. It is expected that this study could improve water supply management and its sustainability. In addition, this could encourage other initiatives in addressing petroleum industry issues associated with the desulfurization of sulfur content.

CRediT authorship contribution statement

Ummi Kalsum Hasanah Mohd Nadzim: Writing – original draft. **Nur Hanis Hayati Hairom:** Conceptualization, Supervision, Funding acquisition, Writing – review & editing. **Mohamad Alif Hakimi Hamdan**: Methodology, Investigation, Data curation. **Mohd Khairul Ahmad:** Conceptualization, Supervision, Methodology. **Aishah Abdul Jalil:** Project administration, Funding acquisition. **Nurfatehah Wahyuny Che Jusoh:** Project administration. **Sofiah Hamzah:** Project administration.

Declaration of Competing Interest

The authors declare that they have no known competing financial interests or personal relationships that could have appeared to influence the work reported in this paper.

Acknowledgments

The authors would like to acknowledge the financial support given by the Ministry of Education Malaysia (MOE) through the Fundamental Research Grant Scheme (FRGS/1/2021/TK0/UTHM/02/14) and Geran Kontrak Kementerian Vot K032. We also would like to thank Universiti Teknologi Malaysia and Universiti Tun Hussein Onn Malaysia (UTHM) for providing Collaborative Research Grant (CRG) 07G66 and GPPS Grant (H601), respectively, for this study.

Appendix A. Supplementary material

Supplementary data associated with this article can be found in the online version at doi:10.1016/j.jallcom.2022.165145.

References

[1] M. Mousavi-Kamazani, Cube-like Cu/Cu2O/BiVO4/Bi7VO13 composite nanoparticles: facile sol-gel synthesis for photocatalytic desulfurization of thiophene under visible light, J. Alloy. Compd. 823 (2020) 153786, https://doi.org/10.1016/j.jallcom.2020.153786
[2] R. Mishra, I. Tomar, S. Singhal, K.K. Jha, Synthesis, properties and biological activity of thiophene: a review, Der Pharma Chem. 3 (2011) 38–54.
[3] O.O. Sadare, F. Obazu, M.O. Daramola, Biodesulfurization of petroleum distillates—current status, opportunities and future challenges, Environments MDPI 4 (2017) 1–20, https://doi.org/10.3390/environments4040085
[4] M.N. Hossain, M.K. Choi, H.S. Choi, A review of the desulfurization processes used for waste tire pyrolysis oil, Catalysts 11 (2021), https://doi.org/10.3390/catal11070801
[5] M.A.H. Hamdan, N.H.H. Hairom, N. Zaiton, Z. Harun, S. Chin Fhong, S.K. Hubadillah, M.R. Jamalludin, N.W. Che Jusoh, A. Abdul Jalil, Photocatalytic degradation of synthetic sulfur pollutants in petroleum fractions under different pH and photocatalyst, Emerg. Adv. Integr. Technol. 02 (2021) 30–38, https://doi.org/10.30880/emait.2021.02.01.004
[6] A. Gnanaprakasam, V.M. Sivakumar, M. Thirumarimurugan, Influencing parameters in the photocatalytic degradation of organic effluent via nanometal oxide catalyst: a review, Indian J. Mater. Sci. 2015 (2015) 1–16, https://doi.org/10.1155/2015/601827
[7] X. Kang, S. Liu, Z. Dai, Y. He, X. Song, Z. Tan, Titanium Dioxide: From Engineering to Applications, 2019. ⟨https://doi.org/10.3390/catal9020191⟩.

[8] A.L. Desa, N.H.H. Hairom, D.A.B. Sidik, N.Z. Zainuri, L.Y. Ng, A.W. Mohammad, N.W.C. Jusoh, A.A. Jalil, Performance of tight ultrafiltration membrane in textile wastewater treatment via MPR system: effect of pressure on membrane fouling, IOP Conf. Ser. Mater. Sci. Eng. 736 (2020), https://doi.org/10.1088/1757-899X/736/2/022033

[9] N. Kamarulzaman, M.F. Kasim, R. Rusdi, Band gap narrowing and widening of ZnO nanostructures and doped materials, Nanoscale Res. Lett. 10 (2015), https://doi.org/10.1186/s11671-015-1034-9

[10] Z. Zang, Efficiency enhancement of ZnO/Cu2O solar cells with well oriented and micrometer grain sized Cu2O films, Appl. Phys. Lett. 112 (2018) 2–8, https://doi.org/10.1063/1.5017002

[11] H. Wang, S. Cao, B. Yang, H. Li, M. Wang, X. Hu, K. Sun, Z. Zang, NH4Cl-modified ZnO for high-performance CsPbIBr2 perovskite solar cells via low-temperature process, Sol. RRL 4 (2020), https://doi.org/10.1002/solr.201900363

[12] H. Wang, P. Zhang, Z. Zang, High performance CsPbBr3 quantum dots photodetectors by using zinc oxide nanorods arrays as an electron-transport layer, Appl. Phys. Lett. 116 (2020), https://doi.org/10.1063/5.0005464

[13] S. Meshram, R. Limaye, S. Ghodke, S. Nigam, S. Sonawane, R. Chikate, Continuous flow photocatalytic reactor using ZnO – bentonite nanocomposite for degradation of phenol, Chem. Eng. J. 172 (2011) 1008–1015, https://doi.org/10.1016/j.cej.2011.07.015

[14] N.H.H. Hairom, A.W. Mohammad, L.Y. Ng, A.A.H. Kadhum, Utilization of self-synthesized ZnO nanoparticles in MPR for industrial dye wastewater treatment using NF and UF membrane, Desalin. Water Treat. 54 (2015) 944–955, https://doi.org/10.1080/19443994.2014.917988

[15] D. Abu, B. Sidik, N. Hanis, H. Hairom, R.M. Adnan, A.S. Afendi, F. Afrina, A. Rahman, N.F. Hisam, Performance of Membrane Photocatalytic Reactor on Palm Oil Mill Secondary Effluent using Zinc Oxide – Cymbopogon citratus (ZnO- CC), 2, 2021, pp. 111–117.

[16] X.M. Gao, F. Fu, L.P. Zhang, W.H. Li, The preparation of Ag-BiVO4 metal composite oxides and its application in efficient photocatalytic oxidative thiophene, Phys. B Condens. Matter 419 (2013) 80–85, https://doi.org/10.1016/j.physb.2013.03.024

[17] A. Tiple, P.S. Sinhmar, P.R. Gogate, Improved direct synthesis of TiO2 catalyst using sonication and its application for the desulfurization of thiophene, Ultrason. Sonochem. 73 (2021) 105547, https://doi.org/10.1016/j.ultsonch.2021.105547

[18] O. Amiri, F. Beshkar, S.S. Ahmed, P.H. Mahmood, A.A. Dezaye, Hierarchical p-BiOI/n-BiPO4 heterojunction nanocomposite with enhanced visible-light photocatalytic desulfurization of thiophene under mild conditions, Int. J. Hydrog. Energy 46 (2021) 6547–6560, https://doi.org/10.1016/j.ijhydene.2020.11.181

[19] M.M. Khan, S.F. Adil, A. Al-mayouf, S.F. Adil, Editorial article metal oxides as photocatalysts, J. Saudi Chem. Soc. (2015) (2015).

[20] C. Karthikeyan, P. Arunachalam, K. Ramachandran, A.M. Al-Mayouf, S. Karuppuchamy, Recent advances in semiconductor metal oxides with enhanced methods for solar photocatalytic applications, J. Alloy. Compd. 828 (2020) 154281, https://doi.org/10.1016/j.jallcom.2020.154281

[21] A. Monshi, M.R. Foroughi, M.R. Monshi, Modified Scherrer equation to estimate more accurately nano-crystallite size using XRD, World J. Nano Sci. Eng. 02 (2012) 154–160, https://doi.org/10.4236/wjnse.2012.23020

[22] R. Bucci, F. Balestrieri, A.D. Magrì, A.L. Magrì, F. Marini, UV–vis spectrophotometric method for the quantitation of all the components of Italian general denaturant and its application to check the conformity of alcohol samples, Talanta 68 (2006) 781–790, https://doi.org/10.1016/J.TALANTA.2005.06.002

[23] J. Fan, T. Li, H. Heng, Hydrothermal growth of ZnO nanoflowers and their photocatalyst application, Bull. Mater. Sci. 39 (2016) 19–26, https://doi.org/10.1007/s12034-015-1145-z

[24] S. Loghambal, A.J.A. Catherine, S.V. Subash, Mathematics and its applications analysis of langmuir-hinshelwood kinetics model for photocatalytic degradation of aqueous direct blue 71 through analytical expression, Int. J. Math. Appl. 6 (2018) 903–913.

[25] I. Udom, Investigation of Enhanced Titanium and Zinc Oxide Semiconductors for the Photodegradation of Aqueous Organic Compounds, 2014.

[26] S. Baruah, J. Dutta, Hydrothermal growth of ZnO nanostructures, Sci. Technol. Adv. Mater. 10 (1) (2009), https://doi.org/10.1088/1468-6996/10/1/013001

[27] V. Shukla, A. Patel, Influence of precursor concentration on CBD grown ZnO thin films, IJSRR 7 (2018) 446–457 ⟨www.ijsrr.org⟩.

[28] B.R. Sankapal, S.D. Sartale, C.D. Lokhande, A. Ennaoui, Chemical synthesis of Cd-free wide band gap materials for solar cells, Sol. Energy Mater. Sol. Cells 83 (2004) 447–458, https://doi.org/10.1016/J.SOLMAT.2004.01.036

[29] N.Z. Zainuri, N.H.H. Hairom, Di.A.B. Sidik, N. Misdan, N. Yusof, A.W. Mohammad, Reusability performance of zinc oxide nanoparticles for photocatalytic degradation of POME, E3S Web Conf. 34 (2018) 1–9, https://doi.org/10.1051/e3sconf/20183402013

[30] Z. Wang, R. Ummethala, N. Singh, S. Tang, C. Suryanarayana, J. Eckert, K.G. Prashanth, Selective laser melting of aluminum and its alloys, Materials (2020) 1–67, https://doi.org/10.3390/ma13204564

[31] S. Harish, M. Navaneethan, J. Archana, A. Silambarasan, S. Ponnusamy, C. Muthamizhchelvan, Y. Hayakawa, Controlled synthesis of organic ligand passivated ZnO nanostructures and their photocatalytic activity under visible light irradiation, Dalton Trans. 44 (2015) 10490–10498, https://doi.org/10.1039/c5dt01572c

[32] G. Amin, M.H. Asif, A. Zainelabdin, S. Zaman, O. Nur, M. Willander, Influence of pH, precursor concentration, growth time, and temperature on the morphology of ZnO nanostructures grown by the hydrothermal method, J. Nanomater. 2011 (2011), https://doi.org/10.1155/2011/269692

[33] R. Wahab, Y.S. Kim, H.S. Shin, Synthesis, characterization and effect of pH variation on zinc oxide nanostructures, Mater. Trans. 50 (2009) 2092–2097, https://doi.org/10.2320/matertrans.M2009099

[34] C. Rassie, R.A. Olowu, T.T. Waryo, L. Wilson, A. Williams, P.G. Baker, E.I. Iwuoha, Dendritic 7T-polythiophene electro-catalytic sensor system for the determination of polycyclic aromatic hydrocarbons, Int. J. Electrochem. Sci. 6 (2011) 1949–1967.

[35] Y. Wang, X. Li, N. Wang, X. Quan, Y. Chen, Controllable synthesis of ZnO nanoflowers and their morphology-dependent photocatalytic activities, Sep. Purif. Technol. 62 (2008) 727–732, https://doi.org/10.1016/J.SEPPUR.2008.03.035

[36] Q. Liang, F. Qiao, X. Cui, X. Hou, Controlling the morphology of ZnO structures via low temperature hydrothermal method and their optoelectronic application, Mater. Sci. Semicond. Process. 89 (2019) 154–160, https://doi.org/10.1016/J.MSSP.2018.09.007

[37] S. Heinonen, J.P. Nikkanen, H. Hakola, E. Huttunen-Saarivirta, M. Kannisto, L. Hyvärinen, M. Järveläinen, E. Levänen, Effect of temperature and concentration of precursors on morphology and photocatalytic activity of zinc oxide thin films prepared by hydrothermal route, IOP Conf. Ser. Mater. Sci. Eng. 123 (2016), https://doi.org/10.1088/1757-899X/123/1/012030

[38] J. Yang, Y. Wang, J. Kong, H. Jia, Z. Wang, Synthesis of ZnO nanosheets via electrodeposition method and their optical properties, growth mechanism, Opt. Mater. 46 (2015) 179–185, https://doi.org/10.1016/j.optmat.2015.04.016

[39] P.M. Aneesh, K.A. Vanaja, M.K. Jayaraj, Synthesis of ZnO nanoparticles by hydrothermal method, Nanophotonic Mater. IV 6639 (2007) 66390J, https://doi.org/10.1117/12.730364

[40] H. Dhasmana, V. Dutta, A. Kumar, A. Kumar, A. Verma, V.K. Jain, Hydrothermally synthesized zinc oxide nanoparticles for reflectance study onto si surface, Mater. Today Proc. 32 (2019) 287–293, https://doi.org/10.1016/j.matpr.2020.01.374

[41] S. Baruah, J. Dutta, Hydrothermal growth of ZnO nanostructures, Sci. Technol. Adv. Mater. 10 (2009), https://doi.org/10.1088/1468-6996/10/1/013001

[42] X. Li, J. Wang, J. Yang, J. Lang, M. Wei, X. Meng, S. Lü, Y. Sui, Enhanced photocatalytic activity of ZnO microflower arrays synthesized by one-step etching approach, J. Mol. Catal. A Chem. 378 (2013) 1–6, https://doi.org/10.1016/J.MOLCATA.2013.05.013

[43] M.G. Kotresh, M.K. Patil, S.R. Inamdar, Reaction temperature based synthesis of ZnO nanoparticles using co-precipitation method: detailed structural and optical characterization, Optik 243 (2021) 167506, https://doi.org/10.1016/j.ijleo.2021.167506

[44] T. Thilagavathi, D. Geetha, Nano ZnO Structures Synthesized in Presence of Anionic and Cationic Surfactant under Hydrothermal Process, (n.d.). ⟨https://doi.org/10.1007/s13204-012-0183-8⟩.

[45] E. Finocchio, C. Cristiani, G. Dotelli, P.G. Stampino, L. Zampori, Thermal evolution of PEG-based and BRIJ-based hybrid organo-inorganic materials. FT-IR, Vib. Spectrosc. 71 (2014) 47–56, https://doi.org/10.1016/j.vibspec.2013.12.010

[46] C. Pholnak, C. Sirisathitkul, S. Suwanboon, D.J. Harding, Effects of precursor concentration and reaction time on sonochemically synthesized ZnO nanoparticles, Mater. Res. 17 (2014) 405–411, https://doi.org/10.1590/S1516-14392013005000192

[47] R. Shah, P.K. Verma, Therapeutic importance of synthetic thiophene, Chem. Cent. J. 12 (2018) 1–22, https://doi.org/10.1186/s13065-018-0511-5

[48] N. Yusof, S. Triwahyono, A.A. Jalil, An interaction study between CO and H2 with fibrous silica KCC-1 by in situ FTIR, Colloquium 13 (2018) 17–20.

[49] S.R.M. Ibrahim, H.M. Abdallah, A.M. El-Halawany, G.A. Mohamed, Naturally occurring thiophenes: isolation, purification, structural elucidation, and evaluation of bioactivities, Phytochem. Rev. 15 (2016) 197–220, https://doi.org/10.1007/s11101-015-9403-7

[50] M. Alhaddad, A. Shawky, Superior photooxidative desulfurization of thiophene by reduced graphene oxide-supported MoS2 nanoflakes under visible light, Fuel Process. Technol. 205 (2020) 106453, https://doi.org/10.1016/j.fuproc.2020.106453

[51] R. Junejo, S. Memon, F.N. Memon, A.A. Memon, F. Durmaz, A.A. Bhatti, A.A. Bhatti, Thermodynamic and kinetic studies for adsorption of reactive blue (RB-19) dye using calix[4]arene-based adsorbent, J. Chem. Eng. Data 64 (2019) 3407–3415, https://doi.org/10.1021/acs.jced.9b00223

[52] J. Thilagan, S. Gopalakrishnan, T. Kannadasan, A Study on Adsorption of Copper (II) Ions in Aqueous Solution by Chitosan – Cellulose Beads Cross Linked by Formaldehyde, 2, 2013, pp. 1043–1054.

[53] G. William Kajjumba, S. Emik, A. Öngen, H. Kurtulus Özcan, S. Aydın, Modelling of adsorption kinetic processes—errors, theory and application, Adv. Sorpt. Process Appl. (2019), https://doi.org/10.5772/intechopen.80495

[54] M.A.H. Hamdan, N.H.H. Hairom, A.A. Jalil, M.K. Ahmad, R.H. Madon, H. Dzinun, S. Hamzah, A.S.M. Kamal, N.W.C. Jusoh, Catalytic conversion of synthetic sulfur-pollutants in petroleum fractions under different photocatalyst loadings and initial concentration, Int. J. Emerg. Trends Eng. Res. 8 (2020) 132–138, https://doi.org/10.30534/ijeter/2020/1881.22020

[55] A.M. Aljeboree, A.N. Alshirifi, A.F. Alkaim, Kinetics and equilibrium study for the adsorption of textile dyes on coconut shell activated carbon, Arab. J. Chem. 10 (2017) S3381–S3393, https://doi.org/10.1016/j.arabjc.2014.01.020

[56] S. Iqbal, A. Bahadur, S. Anwer, S. Ali, R.M. Irfan, H. Li, M. Shoaib, M. Raheel, T.A. Anjum, M. Zulqarnain, Effect of temperature and reaction time on the morphology of L-cysteine surface capped chalcocite (Cu2S) snowflakes dendrites nanoleaves and photodegradation study of methyl orange dye under visible light, Colloids Surf. A Physicochem. Eng. Asp. 601 (2020) 124984, https://doi.org/10.1016/j.colsurfa.2020.124984

[57] H. Moussout, H. Ahlafi, M. Aazza, H. Maghat, Critical of linear and nonlinear equations of pseudo-first order and pseudo-second order kinetic models, Karbala Int. J. Mod. Sci. 4 (2018) 244–254, https://doi.org/10.1016/j.kijoms.2018.04.001